

# GEOMETRIC CORRECTION OF REMOTELY SENSED IMAGES<sup>♥</sup>

Thierry Toutin

Natural Resources Canada, Canada Centre for remote Sensing  
588 Booth Street, Ottawa, Ontario K1A 0Y7  
thierry.toutin@ccrs.nrcan.gc.ca

## 1. INTRODUCTION

Remotely sensed images usually contain geometric distortions so significant that they cannot be used directly with map base products in a geographic information system (GIS). Consequently, multi-source data integration (raster and vector) for cartographic applications, such as forestry, requires geometric and radiometric processing adapted to the nature and characteristics of the data in order to keep the best information from each image in the composite ortho-rectified image.

The processing of multi-source data can be based on the concept of “terrain-geocoded images”, a term originally invented in Canada in defining value-added products (Guertin and Shaw, 1981). Photogrammetrists, however, prefer the term “ortho-image” in referring to the unit of terrain-geocoded data, where all distortions including the relief are corrected. To integrate different data under the concept, each raw image must be separately converted to an ortho-image so that each component ortho-image of data set can be registered, compared, combined, etc. pixel by pixel but also with cartographic vector data in a GIS.

Although geometric corrections have always been present in remotely sensed images, they have become a more significant problem in recent years. In 1972, the impact of the distortions was quite negligible for the following reasons (Toutin, 1996):

- The images, such as Landsat-MSS, were nadir viewing and the resolution was coarse (around 80-100 m);
- The products, resulting from the image processing were analogue on paper;
- The interpretation of the final products was performed visually; and
- The fusion and integration of multi-source and multi-format data did not exist.

Today, however, the impact of distortions is no longer negligible because:

- The images are off-nadir viewing and the resolution is fine (sub-meter level);
- The products resulting from image processing are fully digital;
- The interpretation of the final products is realised on computer;
- The fusion of multi-source images (different platforms and sensors) is in general use; and

---

<sup>♥</sup> Published in *Remote Sensing of Forest Environments: Concepts and Case Studies*, M. A. Wulder and S. E. Franklin Editors, Kluwer Academic Publishers, 2003, Chapter 6, pp. 143-180.

- The integration of multi-format data (raster/vector) is a general tendency in geomatics.

Advances in every aspect of remote sensing —the quality of acquired data, data processing, analysis and interpretation— since the 1970s, have made it ever more important to accurately apply corrections to these geometric corrections.

Although the literature is quite abundant, mainly in term of peer review articles, it is important to update this body of knowledge with the latest developments and research studies from around the world. An exhaustive list of books, journals and papers are given at the end of this Chapter. This Chapter will then address:

- The source of geometric distortions and deformations with different categorisations (section 2);
- The modelling of the distortions with different models and mathematical functions (section 3); and
- The geometric correction method with the processing steps and errors (section 4).

Comparisons between the models and mathematical functions, their applicability and their performance on different types of images (frame camera, Visible and Infra-Red (VIR) oscillating or push-broom scanners, Synthetic Aperture Radar (SAR) sensors, high or medium resolution) are also addressed. The errors, together with their propagation from the input data to the final results, are also evaluated through the full processing steps.

## 2. GEOMETRIC DISTORTIONS AND MODELS

### 2.1 Distortion sources

Each image acquisition system (Figure 6-1) produces unique geometric distortions in its raw images; consequently the geometry of these images does not correspond to the terrain nor to end-user maps. The geometric distortions vary considerably with different factors such as the platform (airborne versus satellite), the sensor (low to high resolution), and also the total field of view. However, it is possible to make general categorisations of these distortions.

The sources of distortion can be grouped into two broad categories: **the Observer** caused by the acquisition system (platform, imaging sensor and other measuring instruments, such as gyroscope, stellar sensors, etc.) and **the Observed** introduced by atmosphere and the Earth. Deformations related to the map projection are also included in **the Observed** distortion category. Terrain and most of GIS end-user applications are generally represented and performed respectively in a topographic space, not in the geoid or a referenced ellipsoid, leading to inconsistencies between maps and remotely sensed data. Table 6-1 describes in more detail the sources of distortion for each category and sub-category. Figures 6-1 and 6-2 illustrate the geometry of acquisition and the elliptical orbit approximation of remote sensing satellites around the Earth, respectively.

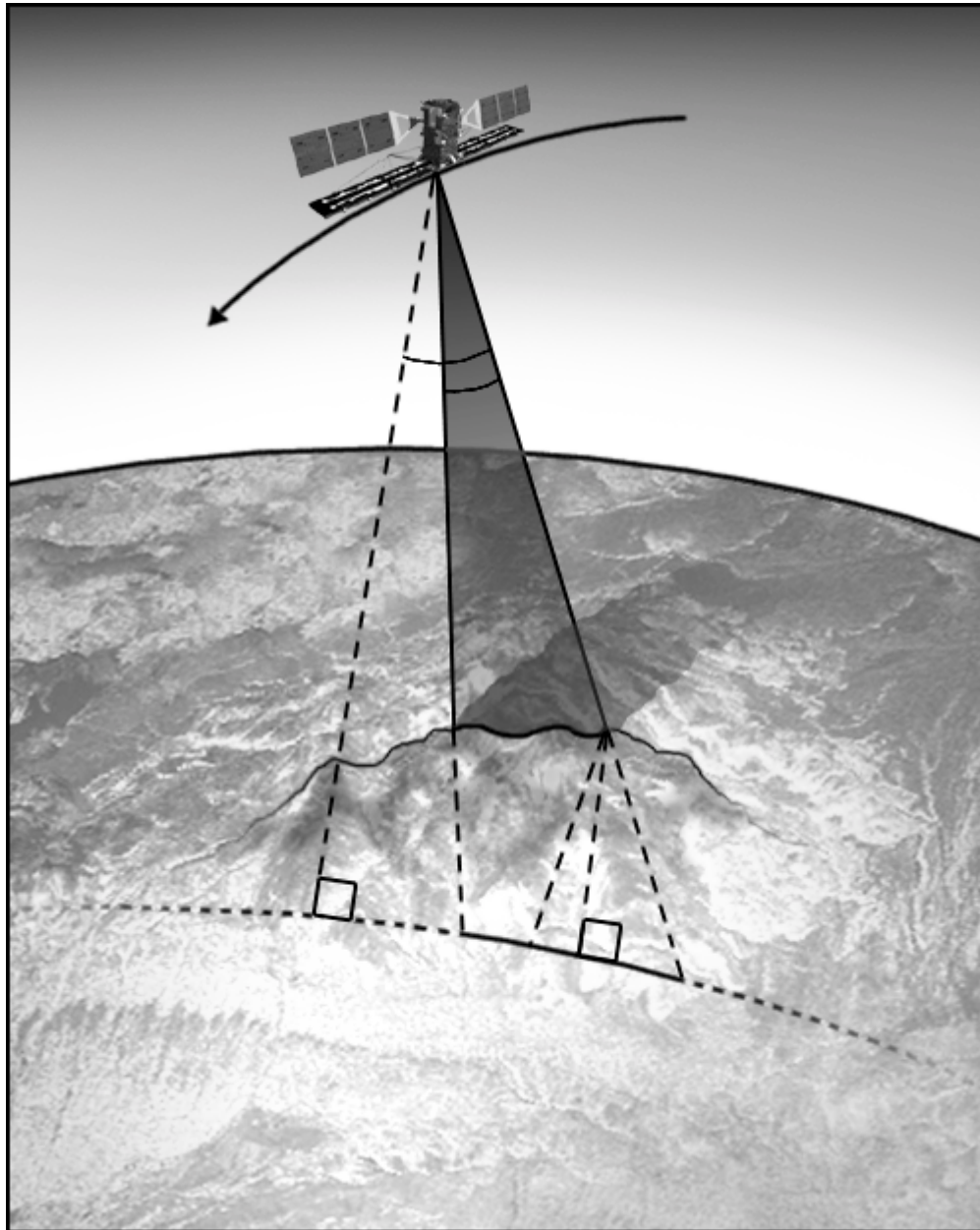


Figure 6-1: Geometry of viewing of a satellite scanner in orbit around the Earth.

Previous studies made a second-level categorisation into low, medium and high frequency distortions (Friedmann *et al.*, 1983), where “frequency” is determined or compared to the image acquisition time. Examples of low, medium and high frequency distortions are orbit variations, Earth rotation, and local topographic effects, respectively. The proliferation of acquisition system designs since the 1980s has, however, rendered this classification obsolete. For example, attitude variation is a high-frequency distortion for Quickbird or airborne push-broom scanner, a medium-frequency distortion for SPOT and Landsat- ETM<sup>+</sup> or a low-frequency distortion for Landsat-MSS.

Table 6-1. Description of error sources for the two categories, *the Observer* and *the Observed*, and the different sub-categories.

CATEGORY	SUB-CATEGORY	DESCRIPTION
<b>The Observer</b>  or  The Acquisition System	Platform	Variation of the elliptic movement (Figure 2) Variation in platform attitude (low to high frequencies)
	Sensor	Variation in sensor mechanics (scan rate, scanning velocity, etc.) Viewing/look angles Panoramic effect with field of view
	Measuring instruments	Time-variations or drift Clock synchronicity
<b>The Observed</b>	Atmosphere	Refraction and turbulence
	Earth	Curvature, rotation, topographic effect
	Map	Geoid to ellipsoid Ellipsoid to map

The geometric distortions of Table 6-1 are predictable or systematic and generally well understood. Some of these distortions, especially those related to the instrumentation, are generally corrected at ground receiving stations or by image vendors. Others, for example those related to the atmosphere, are not taken into account and corrected because they are specific to each acquisition time and location and information on the atmosphere is rarely available. They also are negligible for low-to-medium resolution images.

The remaining distortions associated with the platform (Figure 6-2) are mainly orbit and Earth related (elliptic movement, Earth gravity, shape and movement) (Escobal, 1965; CNES, 1980; Light *et al.*, 1980). Depending of the acquisition time and the size of the image, the orbital perturbations may cause a range of distortions. Some effects include:

- Platform altitude variation in combination with sensor focal length, Earth's flatness and terrestrial relief can change the pixel spacing;
- Platform attitude variation (roll, pitch and yaw) can change the orientation and the shape of VIR images; it does not affect SAR image geometry;
- Platform velocity variations can change the line spacing or create line gaps/overlaps.

The remaining sensor-related distortions include:

- Calibration parameter uncertainty such as in the focal length and the instantaneous field of view (IFOV) for VIR sensors or the range gate delay (timing) for SAR sensors;
- Panoramic distortion in combination with the oblique-viewing system, Earth curvature and topographic relief changes the ground pixel sampling along the column.

The remaining Earth-related distortions include (Figure 6-1):

- Rotation, which generates latitude-dependent displacements between image lines;
- Curvature, which for large width image creates variation in the pixel spacing;
- Topographic relief, which generates a parallax in the scanner direction.

The remaining deformations associated with the map projection are:

- The approximation of the geoid by a reference ellipsoid;
- The projection of the reference ellipsoid on a tangent plane.

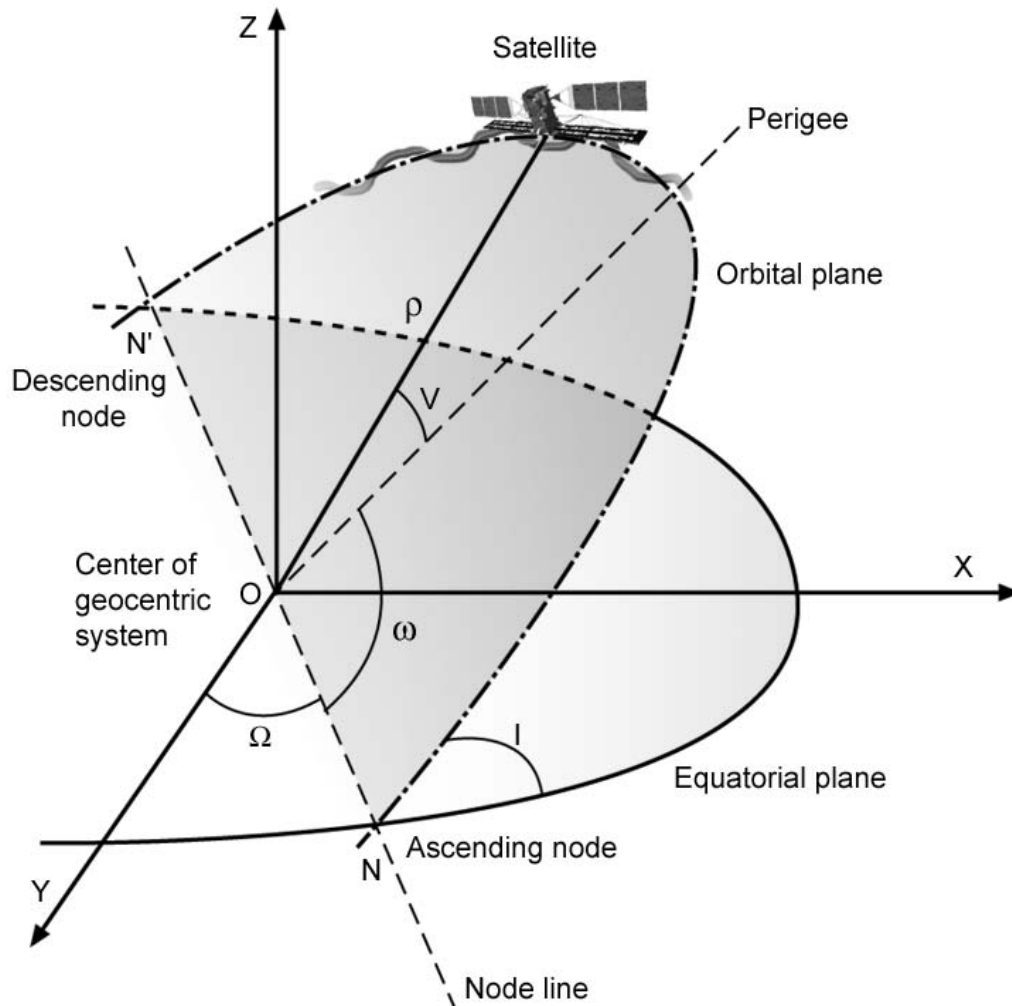


Figure 6-2: Description of a satellite orbit and its approximation by an ellipse.  $XYZ$  are the geocentric frame reference system.  $\Omega$  is the longitude of the ascending node ( $N$ );  $\omega$  is the argument of the perigee ( $P$ );  $(\omega + v)$  is the argument of the satellite;  $\rho$  is the distance from the Earth centre ( $O$ ) and the satellite.

All these remaining geometric distortions require models and mathematical functions to perform geometric corrections of imagery: either through 2D/3D non-parametric models (such as 2D/3D polynomial or 3D rational functions) or with rigorous 3D parametric models. With 3D parametric models, geometric correction can be performed step-by-step with a mathematical function for each distortion or simultaneously with a “combined” mathematical function. The first solution is generally applied at the ground receiving station when the image distributors sell added-value products (georeferenced, map oriented or geocoded) while the end users generally prefer and use the last solution.

## 2.2 2D/3D non-parametric models

The 2D/3D non-parametric models, based on different mathematical functions (Table 6-2), can be used when the parameters of the acquisition systems or a rigorous 3D parametric model are not available. Since they do not reflect the source of distortions described previously, these models do not require *a priori* information on any component of the total system (platform, sensor, Earth and map projection).

*Table 6-2. Mathematical equations and numbers of unknown terms for the different geometric models. For each geometric model there are two equations. In some conditions, specific terms, such as  $XY^2$  for 2D or  $XZ$ ,  $YZ^2$  or  $Z^3$ , etc. for 3D, can be dropped of the polynomial functions, when these terms can not be related to any physical element of the image acquisition geometry; it also reduces correlation between terms.*

Geometric Models	Mathematical Functions* $P_{2D}$ , $P_{3D}$ & $R_{3D}$	Number of unknown terms
2D Polynomial	$P_{2D}(XY) = \sum_{i=0}^m \sum_{j=0}^n a_{ij} X^i Y^j$	1 <sup>st</sup> order: 3 + 3 2 <sup>nd</sup> order: 6 + 6 3 <sup>rd</sup> order: 10 + 10
3D Polynomial	$P_{3D}(XYZ) = \sum_{i=0}^m \sum_{j=0}^n \sum_{k=0}^p a_{ijk} X^i Y^j Z^k$	1 <sup>st</sup> order: 4 + 4 2 <sup>nd</sup> order: 10 + 10 3 <sup>rd</sup> order: 20 + 20
3D Rational	$R_{3D}(XYZ) = \frac{\sum_{i=0}^m \sum_{j=0}^n \sum_{k=0}^p a_{ijk} X^i Y^j Z^k}{\sum_{i=0}^m \sum_{j=0}^n \sum_{k=0}^p b_{ijk} X^i Y^j Z^k}$	1 <sup>st</sup> order: 8 + 8 2 <sup>nd</sup> order: 20 + 20 3 <sup>rd</sup> order: 40 + 40

\* X, Y, Z are the cartographic coordinates; i, j, k are integer increments; m, n and p are integer values, generally comprised between 1 and 3 with m + n + p being the order of the polynomial functions

### 2.2.1 2D Polynomial Functions

Since the 2D polynomial functions, with their formulation, are well known and documented for the last 20 years (Billingsley, 1983), only a few characteristics are given. The polynomial functions of the 1<sup>st</sup> order (6 terms) allow for only correcting a translation in both axes, a rotation, scaling in both axes and an obliquity (Table 6-2). The polynomial functions of the 2<sup>nd</sup> order (12 terms) allow for correction, in addition to

the previous parameters, torsion and convexity in both axes. The polynomial function of the 3<sup>rd</sup> order (20 terms) allows for correction of the same distortions as a 2<sup>nd</sup> order polynomial function with others, which do not necessarily correspond to any physical reality of the image acquisition system. In fact, previous research studies demonstrated that 3<sup>rd</sup> order polynomial functions introduce errors in the relative pixel positioning in ortho-images (Caloz et Collet, 2001) or in geocoding and integration of multi-sensor images (Toutin, 1995a).

Since the 2D polynomial functions do not reflect the sources of distortion during the image formation and do not correct for terrain relief distortions they are limited to images with few or small distortions, such as nadir-viewing images, systematically-corrected images and/or small images over flat terrain. Since these functions correct for local distortions at the ground control point (GCP) location they are very sensitive to input errors; hence GCPs have to be numerous and regularly distributed. Consequently, these functions neither should be used when precise geometric positioning is required for multi-source/multi-format data integration.

The 2D polynomial functions were mainly used in the 70's and 80's on images (Billingsley, 1983), whose systematic distortions, excluding the relief, had already been corrected for by the image providers. As mentioned in the Introduction, a good geometric accuracy was not a key point in the analysis of analogue images. However, while it is now known that 2D polynomial functions are not suitable for accurately correcting remote sensing images, some users still apply them, apparently without knowing implications for subsequent processing operations and resulting digital products. Some comparisons of processing and of results based on 2D polynomial and 3D parametric functions will be provided in a later section.

### 2.2.2 3D Polynomial Functions

The 3D polynomial functions are an extension of the 2D polynomial function by adding Z-terms related to the third dimension of the terrain (Table 6-2). However, apart from relief they are prone to the same problems as other non-parametric functions: i.e. they are applicable to small images, they need numerous regularly distributed GCPs, they correct locally at GCPs, they are very sensitive to errors, they lack robustness and consistency in operational environments. Their use should be thus limited to small images or to systematically correct images, where all distortions except the relief have been pre-corrected.

3D polynomial functions have been recently used with the following georeferenced image data sets: SPOT-HRV (level 1B), Landsat-TM (level bulk or georeferenced) (Palà and Pons, 1995) and IKONOS Geo-products (Hanley and Fraser, 2001). Kratky (1989) used 3<sup>rd</sup> order 3D polynomial functions to approximate a 3D parametric model developed for SPOT raw images in order to reduce the computing time for implementing his solution on-line into a stereo-workstation. One reason was that the real-time computation of his preferred mathematical model was not feasible.

The terms related to terrain elevation in the 3D polynomial function could be reduced to  $a_i Z$  for VIR images and to  $a_i Z$  and  $a_j Z^2$  for SAR images, whatever the order of the polynomial functions used. The main reason is that there is no physical interrelation in the X and Z or Y and Z directions for most of the sensors used.

### 2.2.3 3D Rational Functions

These 3D rational functions have recently drawn interest from the civilian photogrammetric and remote sensing communities due to the launch of the civilian high-resolution IKONOS sensor in 1999, and subsequently EROS-A1 and QuickBird-2 sensors in 2000 and 2001, respectively. The major reason of their recent interest is that Space Imaging does not release information on the IKONOS satellite and the sensor. The 3D rational functions can be used in two ways:

1. To approximate an already-solved existing 3D parametric model; and
2. To normally compute the unknowns of all the polynomial functions with GCPs.

The first approach is performed in two steps. A 3D regular grid of the imaged terrain is first defined and the image coordinates of the 3D grid ground points are computed using the already-solved existing 3D parametric model. These grid points and their 3D ground and 2D image coordinates are then used as GCPs to resolve the 3D rational functions and compute the unknown terms of polynomial functions.

This approach has been proven adequate for aerial photographs and satellite images (Tao and Hu, 2001a). However, they found that the results are very sensitive to GCP distribution for SPOT images. When the image is too large, the image itself has to be subdivided and separate 3D rational functions are required for each sub-image. It sometimes results in “less user-friendly” processing than a 3D parametric model. Image vendors or government agencies that do not want to deliver satellite/sensor information with the image, are the main users of this piecewise approach. They thus provide with the image all the parameters of 3D rational functions. Consequently, the users can directly process the images for generating ortho-images or DEM or even post-process to improve the rational function parameters. This method is recently adopted by Space Imaging to sell their IKONOS Geo images with the 3<sup>rd</sup>-order rational functions parameters (Dial and Grodecki, 2002). However, this approach is considered unsuitable for endusers because it requires the knowledge of a 3D parametric model. In this situation, the user can directly use and apply the 3D parametric model. Furthermore, this approximation of the 3D parametric model will not generally be as precise than the 3D parametric model itself.

The second approach can be performed by the endusers with the same processing method as with polynomial functions. Since there are 40 and 80 parameters for the four 2<sup>nd</sup> and 3<sup>rd</sup> order polynomial functions (Table 6-2), a minimum of 20 and 40 GCPs, respectively are required to resolve the 3D rational functions. However, the rational functions, such as the 2D/3D polynomial functions, do not model the physical reality of the image acquisition geometry and they are sensitive to input errors. Consequently in



an operational environment, many more GCPs will be required to reduce their error propagation.

Rational functions, such as the 2D/3D polynomial functions, mainly correct locally at GCP locations, and the distortions between GCPs are not entirely eliminated. A piecewise approach as described previously should then be used for large images (SPOT, Landsat, IRS), however the number of GCPs will increase proportionally to the number of sub-images, making the method impractical.

In conclusions, the 3D rational functions are certainly the best selection among the non-parametric functions, but only when no 3D parametric solution, such as described below, is available.

## **2.3 3D parametric models**

3D parametric models to perform the geometric correction differ depending on the sensor, the platform and its image acquisition geometry:

- The instantaneous acquisition systems, such as photogrammetric cameras, Metric Camera (MC) or Large Format Camera (LFC);
- The rotating or oscillating scanning mirrors, such as Landsat-MSS, TM or ETM<sup>+</sup>;
- The push-broom scanners, such as SPOT-HRV, IRS-1C/D, IKONOS or Quickbird;
- The SAR sensors, such as ERS-1/2, RADARSAT-1/2 or ENVISAT.

It is possible to create an overall model for the development of 3D parametric functions, which will take into account the unique characteristics of each platform and which will fully correct all distortions described previously. The 3D parametric functions should model the distortions of the platform (position, velocity, attitude for VIR sensors), the sensor (viewing angles, panoramic effect), the Earth (ellipsoid and relief) and the cartographic projection. The geometric correction process can address each distortion one by one and step by step or simultaneously. It is better to consider the overall viewing geometry (platform + sensor + Earth + map), because some of their distortions are correlated and have the same type of impact on the ground. It is theoretically more precise to compute one “combined” parameter only than each component of this “combined” parameter, separately.

Some examples of “combined” parameters include:

- The “orientation” of the image is a combination of the platform heading due to orbital inclination, the yaw of the platform, the convergence of the meridian;
- The “scale factor” in along-track direction is a combination of the velocity, the altitude and the pitch of the platform, the detection signal time of the sensor, the component of the Earth rotation in the along-track direction; and
- The “levelling angle” in the across-track direction is a combination of platform roll, the viewing angle, the orientation of the sensor, the Earth curvature; etc.

Considerable research has been carried out to develop robust and rigorous mathematical models describing the acquisition geometry related to different types of images (VIR

and SAR) and of platforms (spaceborne and airborne) (Table 6-3). The general starting point of these research studies is generally the well-known collinearity condition and equations (Wong, 1980) for VIR images and the Doppler and range equations for radar images (Curlander, 1986) (Table 6-4). It should be noted that the collinearity equations were adapted as radargrammetric equations to process radar images (Leberl, 1972; 1990; Konecny *et al.*, 1986) and later as an integrated and unified mathematic equations to indiscriminately process VIR or radar images (Toutin, 1995b).

*Table 6-3. References on research studies for the development of 3D parametric models applied to different platforms and sensors.*

Platforms and Sensors	Airborne	Spaceborne
Medium Resolution VIR		13, 17, 18, 23, 26, 28, 37, 40, 44, 46, 50, 71
High Resolution VIR	11, 14, 21	10, 57, 59, 63, 66, 67
SAR	8, 15, 24, 29, 30, 42, 62	7, 19, 31, 39, 61

*Table 6-4. 3D parametric models with their mathematical equations for VIR and SAR images (Wong, 1980; Curlander, 1986).*

3D Parametric Models	Mathematical Equations	Description of Parameters
<b>VIR Images</b>  (Collinearity Equations)	$x = -f \frac{m_{11}(X - X_0) + m_{12}(Y - Y_0) + m_{13}(Z - Z_0)}{m_{31}(X - X_0) + m_{32}(Y - Y_0) + m_{33}(Z - Z_0)}$ $y = -f \frac{m_{21}(X - X_0) + m_{22}(Y - Y_0) + m_{23}(Z - Z_0)}{m_{31}(X - X_0) + m_{32}(Y - Y_0) + m_{33}(Z - Z_0)}$	(x, y) the image coordinates (X, Y, Z) the map coordinates (X <sub>0</sub> , Y <sub>0</sub> , Z <sub>0</sub> ) the projection centre coordinates -f the focal length of the VIR sensor [m <sub>ij</sub> ] the 9 elements of the orthogonal 3-rotation matrix
<b>SAR Images</b>  (Doppler-range Equations)	$f = \frac{2(\vec{V}_s - \vec{V}_p) \cdot (\vec{S} - \vec{P})}{\lambda  \vec{S} - \vec{P} }$ $r =  \vec{S} - \vec{P} $	f the Doppler value r the range distance $\vec{S}$ and $\vec{V}_s$ the sensor position and velocity $\vec{P}$ and $\vec{V}_p$ the target-point position and ground velocity $\lambda$ the radar wavelength

The collinearity equations are valid for an instantaneous image or scanline acquisition, such as photogrammetric cameras (LFC, MC), VIR scanner sensors (SPOT, Landsat) and the Doppler-range equations are valid for a SAR scanline. However, since the parameters of neighbouring scanlines of scanners are highly correlated, it is possible to link the exposure centres and rotation angles of the different scanlines to integrate supplemental information, such as:

- The ephemeris and attitude data using celestial mechanic laws (Figure 6-2) for satellite images; or
- The global positioning system (GPS) and inertial navigation system (INS) data for airborne images.

The integration of the different distortions and the derivation of equations for different sensors are outside the scope of this Chapter. They are described for photogrammetric cameras in Wong (1980), for Landsat data in Salamonowicz (1986) and Shu (1987), for SPOT data in Guichard (1983) and Toutin (1983) and for SAR data in Leberl (1972) or Curlander (1982). For example, the solution for the 3D parametric functions given in Guichard (1983) and Toutin (1983, 1995) starts from the collinearity equations written in the instrument reference system. They have been adapted to suit the geometry of scanner imagery, but also have benefited from theoretical work in celestial mechanics to better determine the satellite's osculatory orbit and parameters than simply using a "constant ellipse" orbit (Figure 6-2). The collinearity equations were then converted into the cartographic projection system with elementary transformations (rotations and translations), which are functions of parameters describing the geometric distortions described in a previous Section, namely:

- Rotation from the sensor reference to the platform reference;
- Translation to the Earth's centre;
- Rotation which takes into account the platform time variation;
- Rotation to align the z-axis with the image centre ( $M_0$ ) on the ellipsoid;
- Translation to the image centre ( $M_0$ );
- Rotation to align the y-axis in the meridian plane;
- Rotation to have  $xM_0y$  tangent to the ellipsoid;
- rotation to align the x-axis in the image scan direction; and
- rotation-translation into the cartographic projection.

The final results, which link the 3D cartographic coordinates to the image coordinates, are two equations:

$$Pp + y(1 + \delta\gamma X) - \tau H - H_0\Delta T^* = 0 \quad (1)$$

$$X + \theta \frac{H}{\cos\chi} + \alpha q(Q + \theta X - \frac{H}{\cos\chi}) - Q\Delta R = 0 \quad (2)$$

with:

$$X = (x - ay)(1 + \frac{h}{N_0}) + by^2 + cxy \quad (3)$$

$$H = h - \frac{x^2}{2N_0} \quad (4)$$

Each parameter has a mathematical parametric formula (Toutin, 1983) that represents the physical realities of the full viewing geometry (satellite, sensor, Earth, map projection):

$H$	is the altitude of the point corrected for Earth curvature;
$H_0$	is the satellite elevation at the image centre line;
$N_0$	is the normal to the ellipsoid;

$a$	is a function of the rotation of the Earth;
$\alpha$	is the instantaneous field-of-view ;
$p, q$	are the image coordinates;
$P, Q$	are the scale factors in Y and X, respectively;
$\tau$ and $\theta$	are a function of the levelling angles in Y and X, respectively;
$\Delta T^*$ and $\Delta R$	are the non-linear variations in attitude if they exist ( $\Delta T^*$ : combination of pitch and yaw, $\Delta R$ : roll);
$x, y$ and $h$	are the ground coordinates;
$b, c, \chi, \delta\gamma,$	are known 2 <sup>nd</sup> order parameters.

## 2.4 Comparisons of non-parametric and parametric models

Table 6-5 summarises the main characteristics and comparisons of the 2D/3D non-parametric methods and the 3D parametric methods. The main differences between 2D and 3D models are noted **in bold type**. Some major differences between non-parametric and parametric models are noted *in italic type*, which enables the 3D parametric models to be more consistent and robust. The 2D/3D differences are mainly related to the capability of 3D models to integrate the terrain elevation information in the different processing steps:

- By adding the Z- elevation to the GCPs; and
- By adding DEM or a mean elevation in the rectification process.

*Table 6-5: Comparison of the different characteristics between 2D/3D non-parametric models and 3D parametric models.*

2D/3D Non-Parametric Model	3D Parametric Model
Does not respect the viewing geometry	Respects the viewing geometry
Not related to geometric distortions	<i>Reflects the geometric distortions</i>
Do not use metadata (ephemeris and attitude)	<i>Uses metadata</i> (ephemeris and attitude)
2D models do not use terrain elevation	<b>Uses terrain elevation information</b>
Corrects image locally at GCPs	Corrects the image globally
Does not filter blunders	<i>Filters blunders</i> with the knowledge of the geometry
Individual adjustments of one image	Simultaneous adjustment of more than one image
Image-to-image correction	Image-to-ground correction
Needs many (>20-60) GCPs	Need few (3-8) GCPs
Sensitive to GCPs distribution	Not sensitive to GCPs distribution
Problem of choice for tie points	GCPs choice as a function of each image

Furthermore, in order to make a qualitative comparison between non-parametric and parametric models, the two extreme models (2<sup>nd</sup>-order 2D polynomial and 3D parametric) were applied to a data fusion of panchromatic SPOT-image and two airborne SAR images (C-band and HH-polarization) (Figure 6-3). These results are used from a previous research study over Sherbrooke, Quebec with 200-m elevation topography (Toutin, 1995a). Figure 6-3 shows a composite image using IHS transformation (assigning SPOT-PLA to hue and the two other airborne SAR to intensity and saturation). They were rectified with a 3D parametric model using a DEM (top) and 2D non-parametric model (bottom). The road vector (accuracy of 3-5 m) has also been registered on each sub-image. The radiometric processing operations performed (HIS, LUT, etc.) are exactly the same for both sub-images, only the geometric processing differs.

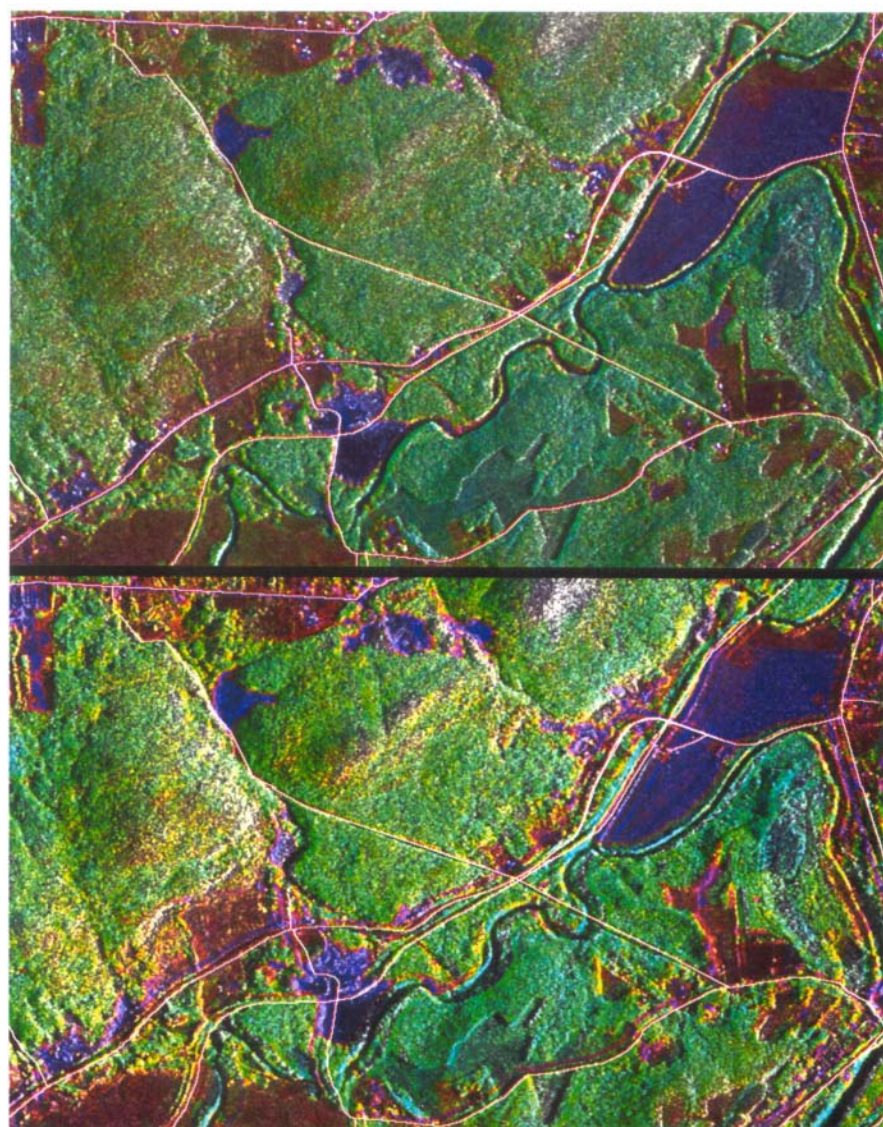


Figure 6-3: Composite sub-ortho-images (4 by 3 km; 5-m pixel spacing) of SPOT-PLA and two C-HH SAR airborne images using IHS transformation with the overlay of digital road network files: processed with 2D 2<sup>nd</sup>-order polynomial method (below), and 3D parametric method (above). SPOT Image © CNES, 1996

The top image is much more homogeneous in its colours, surfaces and variations. As there is greater contrast between the elements, their boundaries are clear and well defined. In the bottom image, the colour variations are greater, giving an impression of texture, and the image seems more blurred. As there is less contrast between the elements, they appear less well defined. Using the vector file from the topographic map, the analysis of certain cartographic elements showed, in the bottom image (letters a to d refer to parts of the image identified in Figure 6-3), that:

- a: The linear elements (roads and rivers) are doubled or even disappear (bridge, roads), which corresponds to a relative error of registration;
- b: The lack of sharpness in this part prevents us from distinguishing the road from the forest and areas of bare soil;
- c: On surface elements, artefacts are created; there is an inversion between forest (green) and cutovers (burgundy);
- d: The texture and colour variations do not correspond to the real information.

These examples, with other similar ones, which can be clearly identified on these sub-images, show that geometric registration errors have generated radiometric merging errors, artefacts and erroneous information in the composite image, which do not correspond to any physical reality.

The road vector file, registered to these sub-images, allows us to check the geometric accuracy. Visual analysis confirms the earlier statistical error results for the polynomial method (30-50 m), but shows an improvement for the photogrammetric method (10 m), with maximum errors of 20 metres. Checks on other parts of images illustrate the consistency of the results. These values correspond to the absolute error of registration. Since these tests and comparisons were performed on small sub-images over rolling topography, the differences will be then more pronounced on larger images rougher over topography.

The general superiority of 3D parametric modeling over non-parametric modeling is mainly due to the fact that the 3D mathematical functions correspond to the physical reality of the viewing geometry and take into account all the distortions generated in the image formation. It is thus more robust in an operational environment to detect errors. Since all the parameters have a physical meaning, they are also easy to interpret when bad or erroneous results occur.

Previous research studies with medium-resolution images (Salamonowicz, 1986; Novak, 1992; Toutin, 1995a; de Sève *et al.*, 1996), review papers and books (Leberl, 1990; Bannari *et al.*, 1995; Calloz et Collet, 2001) are all in agreement with these above statements. More recently with high-resolution images, 3D rational models show worse and less consistent results (Toutin *et al.*, 2002) and some inconsistencies in the results were not explained (Davis and Wang, 2001). Table 6-6 gives comparisons for the three new high-resolution sensors geometrically processed with 3D rational functions and 3D parametric functions. They are the statistical results (root mean square and maximum errors in metres) computed on Independent Check Points (ICPs) from 3D 1<sup>st</sup>-order rational model and 3D parametric model adjustment for EROS A1, IKONOS and QuickBird-2 (Toutin *et al.*,

2002). The results on ICPs for the 3D parametric models are always two-to-three times better than with 3D 1<sup>st</sup>-order rational models. However, other studies demonstrated the feasibility of 3D non-parametric models with high-resolution images, only in a well-controlled research environment with only one image acquired over a flat terrain (Hanley and Fraser, 2001; Tao and Hu, 2001b) but rarely or never realized by end-users in an operational environment. More research should be thus performed to evaluate the true applicability and the limitations of these 3D rational functions for high-resolution images.

*Table 6-6: Results (root mean square and maximum errors in metres) computed on Independent Check Points (ICPs) from 3D 1<sup>st</sup>-order rational model and 3D parametric model adjustment for EROS A1, IKONOS and QuickBird-2 images (Toutin et al., 2002).*

<b>High-resolution Image Correction Model</b>	<b>RMS Errors (m)</b>		<b>Maximum Errors (m)</b>	
<b>EROS A1</b>	<i>X</i>	<i>Y</i>	<i>X</i>	<i>Y</i>
3D 1 <sup>st</sup> -order Rational	8.0	13.2	20	23
3D Parametric	<b>3.9</b>	<b>3.5</b>	<b>6.2</b>	<b>6.0</b>
<b>IKONOS</b>				
3D 1 <sup>st</sup> -order Rational	2.2	5.2	5.1	10.4
3D Parametric	<b>1.3</b>	<b>1.3</b>	<b>3.0</b>	<b>3.0</b>
<b>QuickBird-2</b>				
3D 1 <sup>st</sup> -order Rational	4.0	2.1	9.5	4.3
3D Parametric	<b>1.4</b>	<b>1.3</b>	<b>2.5</b>	<b>2.8</b>

These arguments presented in these research studies to support the 3D rational models as *Universal Sensor Model* include simplified mathematical functions, easier to use, fast computation and universality of its form due to sensor independence (frame camera, scanner) (Madani, 1999). Since no application with SAR or airborne scanner sensors and very few with medium-to-high resolution VIR sensors were performed, can 3D rational models be called a *Universal Sensor Model*? Furthermore, Madani (1999) also addressed their disadvantages:

- Inability to model local distortions (such as with CCD arrays or worse with SAR sensors);
- Limitation in the image size;
- Difficulty in the interpretation of the parameters due to the lack of physical meaning;
- Potential failure to zero denominator; and
- Potential correlation between the terms of polynomial functions.

Furthermore, the arguments of simplified mathematical functions and of universality, easy to develop and to use, can also be applied to already-existing 3D parametric models. In fact, some of 3D parametric models were “mathematically generalized” (Leberl, 1972; Masson d’Autumne, 1979; Konecny, 1986; Toutin, 1995b) and they have all these advantages in addition to the general advantages previously mentioned for 3D parametric models.

In these conditions, 3D rational models should mainly be used when **no** 3D parametric models has been developed. In fact, the parameterisation of models has always been a major issue in scientific research and achievements. When it becomes theoretically and/or practically impossible, statistical methods such as 3D rational models take over.

### 3. METHODS, PROCESSING AND ERRORS

Whatever the mathematical functions used, the geometric correction method and processing steps are more and less the same. The processing steps are (Figure 6-4):

- Acquisition of image(s) and *pre-processing of meta data*;
- Acquisition of the ground points (control/check/pass) with image coordinates and map coordinates X, Y, (**Z**);
- Computation of the unknown parameters of the mathematical functions used for the geometric correction model for one or more images;
- Image(s) rectification **with or** without DEM.

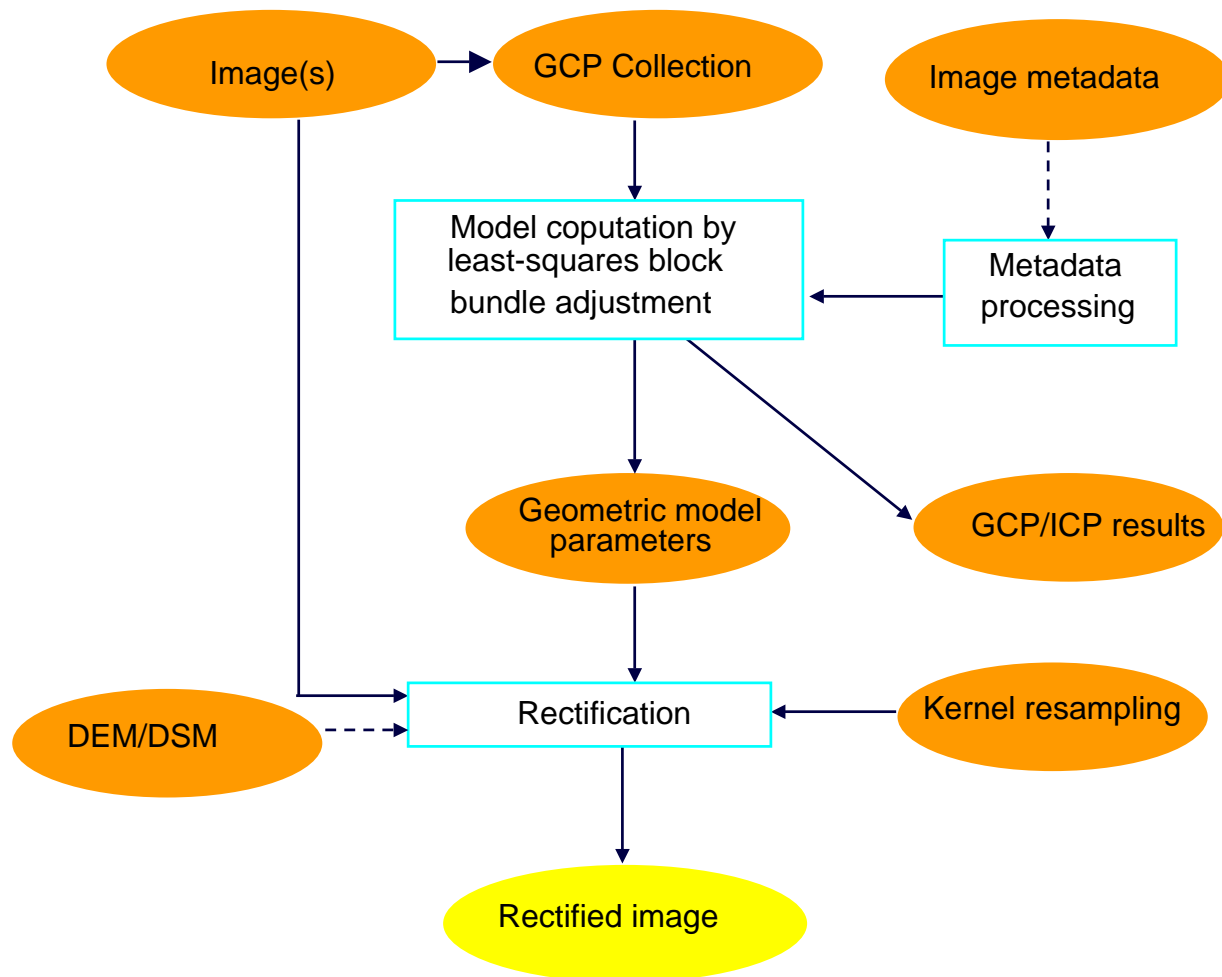


Figure 6-4: Description of the geometric correction method and processing steps. The ellipse symbols are input/output data and the box symbols are processes.



The main differences in the processing steps between non-parametric and parametric models are *in italic style* and between 2D non-parametric and 3D models are **in bold style**. The metadata are useless for non-parametric models because the models do not reflect the geometry of viewing, while the Z-elevation coordinates for GCPs and DEM/DSM are of no use for 2D non-parametric models.

### 3.1 Acquisition of images and metadata

With VIR images, different types of image data with different levels of pre-processing can be obtained, but more the image providers unfortunately use a range of terminology to denominate the same type of image data. Standardization should be better defined, mainly for the convenience of end-users:

- Raw images with only normalization and calibration of the detectors (e.g. level 1A for SPOT or 1B for QuickBird-2) without any geometric correction are satellite-track oriented. In addition, full metadata related to sensor, satellite (ephemeris and attitude) and image are provided;
- Geo-referenced images (e.g. level 1B for SPOT or 1G for Landsat-ETM<sup>+</sup>) corrected for systematic distortions due to the sensor, the platform and the Earth rotation and curvature are satellite-track oriented. Generally, few metadata related to sensor and satellite are provided; some of metadata are related to the 1B processing; or
- Map-oriented images, also called geocoded images, (e.g. level 2A for SPOT or Cartera Geo for IKONOS) corrected for the same distortions as geo-referenced images are North oriented. Generally, very few metadata related to sensor and satellite are provided; most of metadata are related to the 2A processing and the ellipsoid/map characteristics.

For the sake of understanding, the easiest terminology defined for SPOT images are used. The raw “level 1A” images are preferred by photogrammetrists because 3D parametric models derived from co-linearity equations are well known and developed and easily used in softcopy workstations. Since different 3D parametric models are largely available for such VIR images, raw 1A-type images should be now favoured by the remote sensing community too. Specific software to read and pre-process the appropriate metadata (ephemeris, attitude, sensor and image characteristics) have to be realized for each image sensor according to the 3D parametric model used. Using celestial mechanics laws and Lagrange equations (Escobal, 1965; CNES, 1980; Light *et al.*, 1980) the ephemeris (position and velocity) can be transformed into osculatory orbital parameters (Figure 6-2) (Toutin, 1983). Since the Lagrange equations take into account the variation of the Earth gravitational potential to link the different positions of the satellite during the image formation, it is more accurate and robust than using a constant ellipse with 2<sup>nd</sup>-order time-dependent polynomial functions (Guichard, 1983; Toutin, 1983; Bannari *et al.*, 1995). This statement is more applicable when long images from a same orbit are used with path processing (Toutin, 1985; Sakaino *et al.*, 2000) or a block bundle adjustment method (Veillet, 1991; Toutin *et al.*, 2001a; Toutin, 2003a). 3D parametric models also well applied to high-resolution airborne images

(Gibson, 1984; Ebner and Muller, 1986) or spaceborne images, such as QuickBird-2 (Toutin and Cheng, 2002) for achieving pixel accuracy or better. Some results were presented using 3D rational functions with raw SPOT images (Tao and Hu, 2001a), but not with high-resolution spaceborne or airborne images.

Since they have been systematically corrected and georeferenced, the “level 1B” images just retain the terrain elevation distortion, in addition to a rotation-translation related to the map reference system. A 3D 1<sup>st</sup>-order polynomial model with Z-elevation parameters could thus be efficient depending of the requested final accuracy. For scanners with across-track viewing capability, only the Z-elevation parameter in the X-equation is useful. The 2<sup>nd</sup>-order non-parametric models could also be used (Palà and Pons, 1995) for correcting some residual errors of the 1B processing. When possible, solutions to overcome the non-parametric model approximation are either to convert the 1B-images back into 1A-images using the metadata and the reverse transformation (Al-Roussan *et al.*, 1997), or to “re-shape and re-size” the 1B-images to the raw imagery format (Valadan Zoej and Petrie, 1998). This 1B-geometric modelling can be mathematically combined with normal 1A 3D parametric model to avoid multiple image resampling. Although this mathematical procedure used for 1B images works better than non-parametric models, it is still recommended that raw images with 3D rigorous parametric models (co-linearity equations) be directly used.

The map-oriented images (“level 2A”) also retain the elevation distortion but image lines and columns are no more related to sensor-viewing and satellite directions. A 3D 1<sup>st</sup>-order polynomial model with Z-elevation parameters in both axes can thus be efficient depending of the requested final accuracy. Such as for level 1B, 2<sup>nd</sup>-order non-parametric models (polynomial or rational) can be used for correcting some residual errors of the 2A processing, but it is generally no longer possible to convert back the 2A image with the reverse transformation. These 2D/3D non-parametric models were recently applied with IKONOS Geo images to achieve pixel accuracy or better:

- 2D first-order polynomial and rational models (Hanley and Fraser, 2001);
- 3D first-order polynomial models (Fraser *et al.*, 2002);
- 3D third-order rational models by Space Imaging using the 1<sup>st</sup> approach (described in 2.2.3) with coefficients computed from their camera model (Dial and Grodecki, 2002);
- 3D 1-order rational models using the 2<sup>nd</sup> approach (described in 2.2.3) with computation of the model parameters using GCPs (Tao *et al.*, 2001b).

Although the results, generally achieved in a well-controlled research environment using (sub-)images acquired over flat terrain, are in the order of pixel accuracy or sometimes better due to good quality of cartographic data, no results, to our knowledge, were published with IKONOS images in high relief terrain. Care must be then taken by end users in the extrapolation of these results to any image acquired over any terrain and processed with any cartographic data.

However, a 3D parametric model has been still approximated and successfully developed for IKONOS Geo images using basic information of the metadata and

celestial mechanics laws and applied to various images acquired over flat-to-rough topography (Toutin and Cheng, 2000; Toutin, 2003b). Even approximated, this 3D parametric model (“using a global geometry and adjustment”) has been proven to be more robust (Toutin *et al.*, 2002) and to achieve more consistent results over the entire image than 3D rational models (“using a local adjustment”) (Davis and Wang, 2001).

SAR images are standard products in slant or ground range presentations. They are generated digitally during post-processing from the raw signal SAR data (Doppler frequency, time delay). Errors present in the input parameters related to image geometry model will propagate through to the image data. These include errors in the estimation of slant range and of Doppler frequency and also errors related to the satellite's ephemeris and the ellipsoid. Assuming the presence of some geometric error residuals, the parameters of a 3D parametric model reflect these residuals. As mentioned previously, the 3D parametric model starts generally either from the traditional Doppler and range equations (Curlander, 1982), from the equations of radargrammetry (Leberl, 1990), or from generalized equations (Leberl, 1972; Toutin, 1995b). Due to the large elevation distortions in SAR images, 2D polynomial models cannot be used, even in rolling topography (Toutin, 1995a) or to extract planimetric features (de Sève *et al.*, 1996). Furthermore, since different 3D SAR parametric models are largely available, no attempt has been done, to our knowledge, to apply 3D polynomial or rational models to SAR images (spaceborne or airborne).

### 3.2 Acquisition of GCPs

Whatever the VIR and/or SAR geometric model used, some GCPs have to be acquired to refine the parameters of the mathematical functions with a least-square adjustment process in order to obtain a cartographic standard accuracy. The number of GCPs is a function of different conditions: the method of collection, the sensor type and resolution, the image spacing, the geometric model, the study site, the physical environment, the GCP definition, the map accuracy and the final expected accuracy.

Figures 6-5 to 6-7 are GCP examples for different sensors (Landsat-7 ETM<sup>+</sup>, RADARSAT-SAR fine mode and IKONOS) in different contexts (flat to mountainous terrain, urban or rural environment). If GCPs are determined *a priori* without any knowledge of the images to be processed 50% of the points may be rejected (Toutin and Carbonneau, 1989). If GCPs are determined *a posteriori* with knowledge of the images to be processed, the reject factor will be smaller (20-30%). Consequently, all the aspects of GCP collection do not have to be considered separately, but as a whole to avoid too large discrepancies in accuracy of these different aspects. For example, do not use GPS survey to process Landsat data in mountainous study site, or do not use road intersection and 1: 50,000 topographic maps to process IKONOS images if you expect 1-2 m final accuracy, etc. The weakest aspect in GCP collection, which is of course different for each study site and image, will thus be the major source of error in the error propagation and overall error budget of the bundle adjustment.

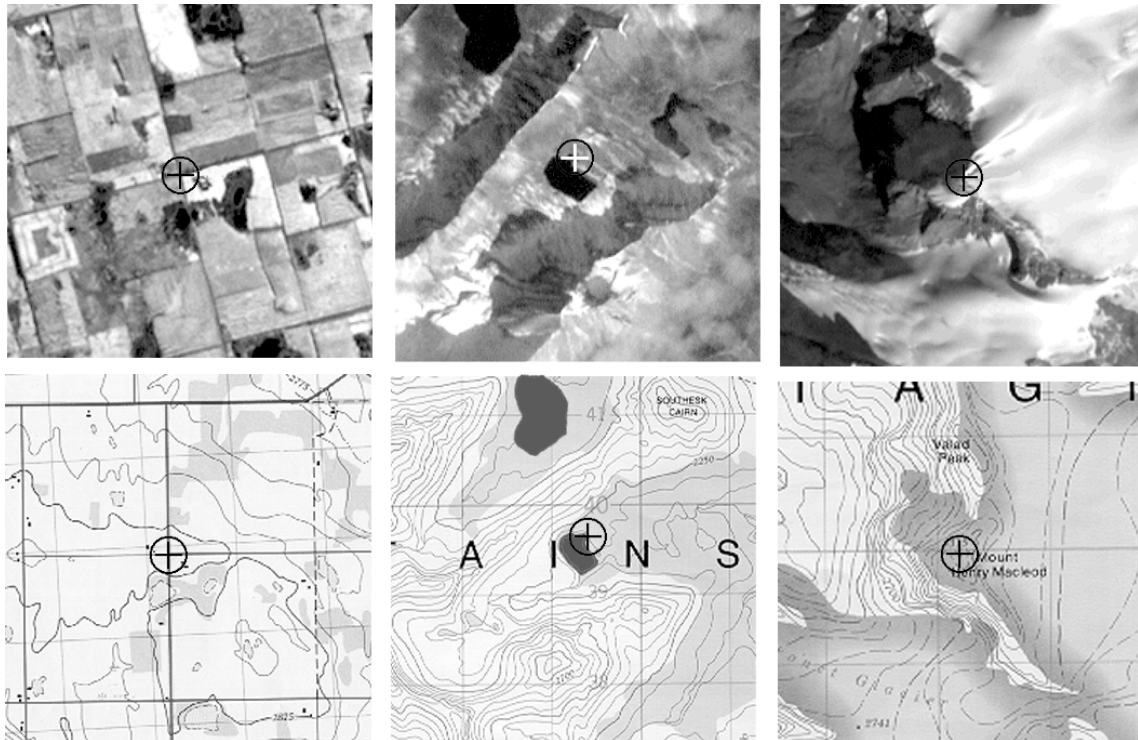


Figure 6-5: Three examples of GCP collection for Landsat-7 ETM<sup>+</sup> images with different features and accuracy and their respective location on 1:50,000 topographic map. A road intersection with better than one-pixel accuracy (left); a lake feature with one-to-two pixel accuracy (centre); the top of a mountain with better two-to-three pixel accuracy (right) and its location on 1:50,000 scanned topographic map.

Since non-parametric models do not reflect the geometry of viewing and do not filter errors, many more GCPs than the theoretical minimum are required to reduce the propagation of input errors in the geometric models. When the map and positioning accuracy is in the same order of magnitude as the image resolution, twice as many is a minimum requirement: around 20, 40 or 80 GCPs should then be acquired for 2<sup>nd</sup>-order 2D polynomial, 3D polynomial or 3D rational models respectively. The 3<sup>rd</sup>-order models obviously required more, mainly the rational functions. Furthermore, to insure robustness and consistency in an operational environment, it is safer to collect more than twice the minimum required mentioned previously. It is then a restriction in the use of such non-parametric models. When more than one image is processed, each image requires its own GCPs and the geometric models are generally computed separately, which does not set-up a relative orientation or link between the images. GCPs should be spread over the full image(s) in planimetry and also in the elevation range for the 3D models. It is also better to have medium-accurate GCPs than no GCP at the tops of mountains, such as it is shown with Landsat-7 (Figure 6-5, right). If the image is larger than the study site it is recommended to reduce the GCP collection to the study site area because the non-parametric models only correct locally.



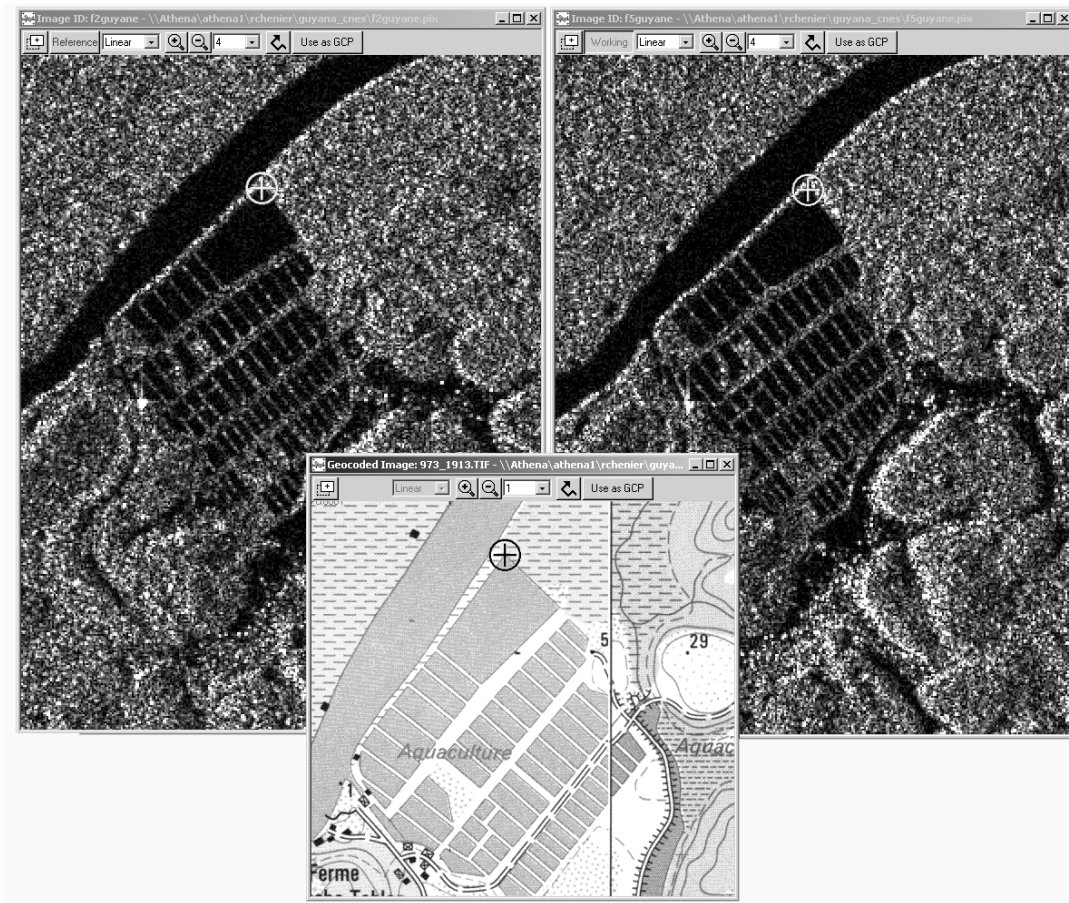


Figure 6-6: Example of stereo GCP collection on RADARSAT-SAR fine mode stereo-images: a field corner with one-to-two pixel accuracy and its location on 1:20,000 scanned topographic map. RADARSAT Images © Canadian Space Agency, 2001

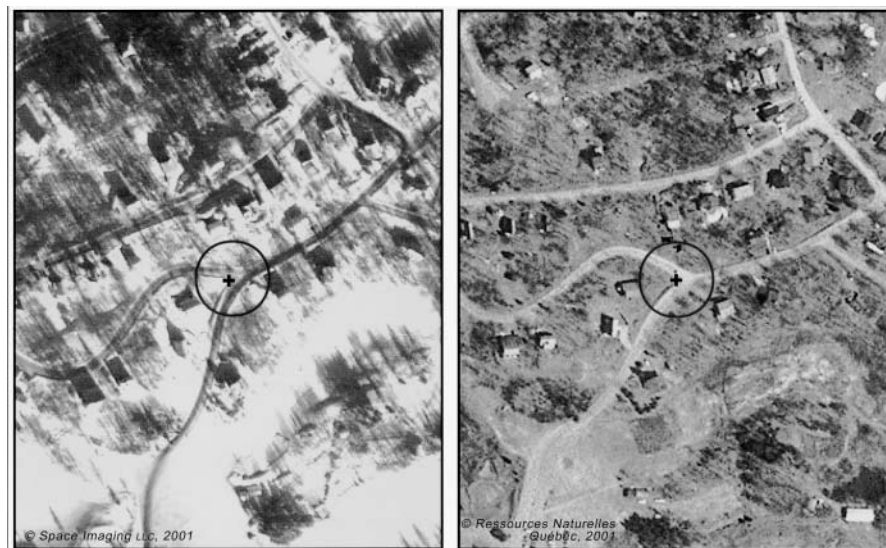


Figure 6-7: Example of GCP collection on IKONOS image: a sidewalk corner with one-to-two pixel accuracy and its location on digital 1-m pixel ortho-photo. It is more precise than the road intersection. IKONOS Images © Space Imaging LLC, 2000

With 3D parametric models, few GCPs (1 to 6) are required per image. When more than one image is processed a spatio-triangulation method with 3D block-bundle adjustment can be used to process all images together (VIR and SAR). It enables users to drastically reduce the number of GCPs for the block with the use of tie points (TPs) (Veillet, 1991; Sakaino *et al.*, 2000; Toutin *et al.*, 2001a, b; Dial and Grodecki, 2002). When the map and positioning accuracy is of the same order of magnitude as the image resolution, twice (or a little less) the theoretical minimum is recommended. When the accuracy is worse, the number should be increased depending also of the final expected accuracy (Savopol *et al.*, 1994). Since more confidence, consistency and robustness can be expected with parametric models (global image processing, filtering input errors) than with non-parametric models, it is not necessary to increase the number of GCPs in operational environments. GCPs should preferably be spread at the border of the image(s) to avoid extrapolation in planimetry, and it is also preferable to cover the full elevation range of the terrain (lowest and highest elevations). Contrary to non-parametric models, it is not necessary to have a regular distribution in the planimetric and elevation ranges. Since the parametric models correct globally the GCP collection has to be performed in the full image size, even if the study site is smaller. First, it will be easier to find GCPs over the full image than over a sub-area and more homogeneity is thus obtained in the different area of the image.

GCP cartographic co-ordinates can be obtained from global positioning system (GPS), air photo surveys, paper or digital maps, ortho-rectified images, chip data base, etc. The cartographic co-ordinates obtained from these sources have drastically different accuracies: from better than 1 m with GPS to 25-50 m with paper maps, certainly the most common GCP source used around the world. Consequently, with lower accuracy more GCPs must be used (Savopol *et al.*, 1994). The image co-ordinates are plotted interactively on the screen or automatically using GCP chip database and image correlation tools. When more than multiple image with overlapping coverage are processed the image co-ordinates are obtained simultaneously in “double monoscopy” because some workstations do not have full stereoscopic capabilities for multi-sensor images. This plotting will then create artificial X- and Y-parallaxes (few pixels) between the images, and the parallax errors will propagate through the bundle adjustment (relative and absolute orientations). The error propagation is larger with SAR images than with VIR images due to a lower plotting accuracy (1-2 pixels versus 1/3-1/2 pixel), and increases with smaller intersection angles, but also with shallower same-side SAR look angles (Toutin, 1998; 1999). Consequently when possible, true stereoscopic plotting using human depth perception, which enables a better relative correspondence of the GCP between the images and a better absolute positioning on the ground, should be used.

### **3.3 Geometric model computation by least-square adjustment**

When more than one image (VIR or SAR) is processed, a spatio-triangulation process based on a block adjustment can be applied to simultaneously compute all geometric models (Figure 6-4). Figure 6-8 is an example of a block over the Canadian Rocky Mountains (BC) with 15 Landsat-ETM<sup>+</sup> images using three rows and five strips (Toutin



*et al.*, 2001b). All model parameters of each image/strip are determined by a common adjustment so that the individual models are properly tied in and the entire block is optimally oriented in relation to the GCPs. With the spatio-triangulation process, the same number of GCPs is theoretically needed to adjust a single image, an image strip or a block. However, some tie points (TPs) between the adjacent images have to be used to link the images and/or strips. Elevation of TPs (ETPs) must be added when the intersection geometry of the adjacent images is weak, such as with intersection angles less than 15°-20° (Toutin *et al.*, 2001a, b). There are a number of advantages to the spatio-triangulation process, namely to:

- Reduce the number of GCPs;
- Obtain a better relative accuracy between the images;
- Obtain a more homogeneous and precise mosaic over large areas; and
- Generate homogeneous GCP network for future geometric processing.

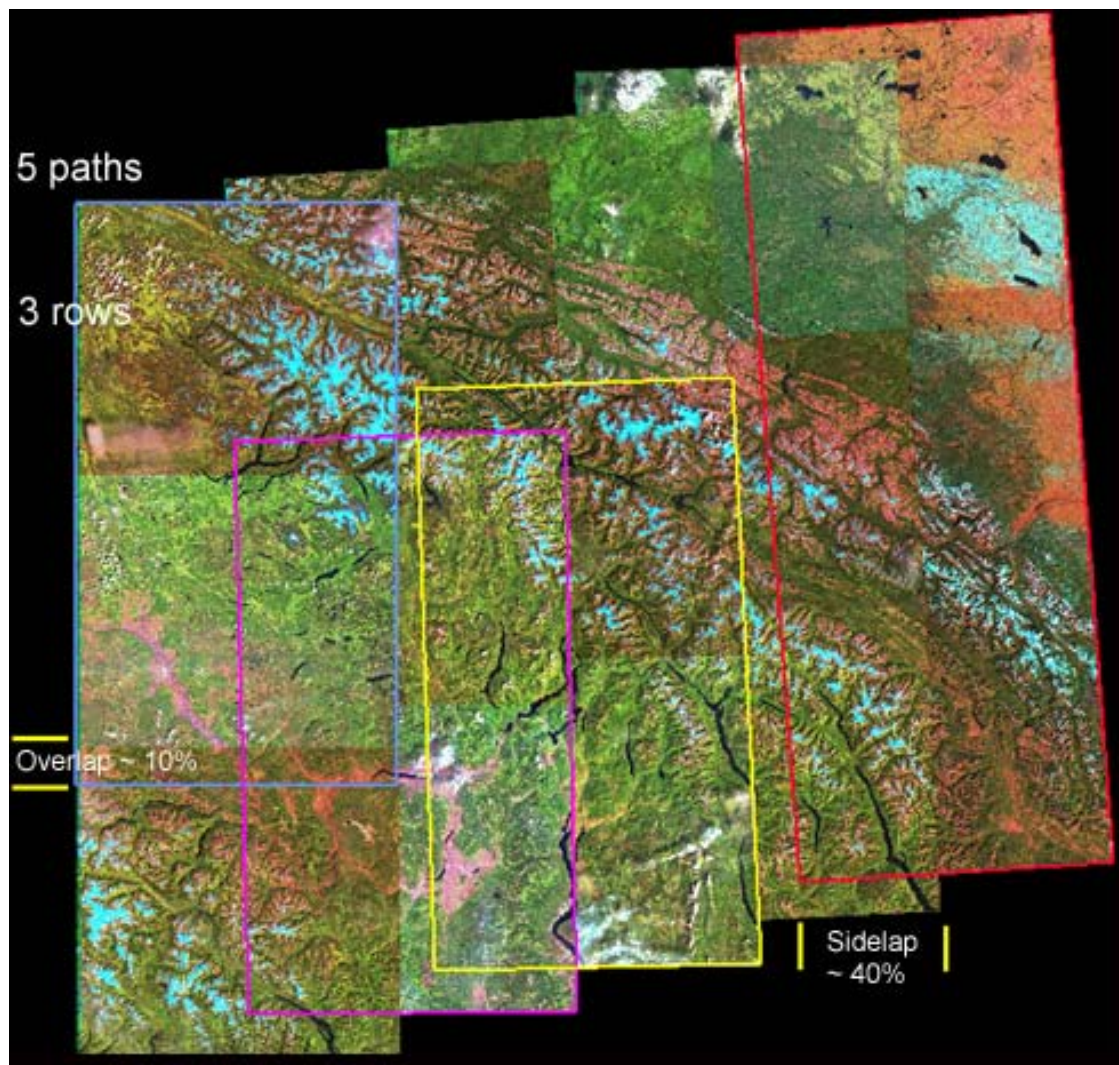


Figure 6-8: Image block of 15 Landsat-7 ETM<sup>+</sup> images over Rocky Mountains, Canada generated from five strips and 3 rows. The lined images are acquired from the same orbit and date and can be used as a single image with path processing.

Whatever the number of images (spatio-triangulation or single image) and the geometric models (parametric or non-parametric) used, each GCP contributes to two observation equations: an equation in X and an equation in Y. The observation equations are used to establish the error equations for GCPs, TPs, and ETPs. Each group of error equations can be weighted as a function of the accuracy of the image and cartographic data. The normal equations are then derived and resolved with the unknowns computed. In addition for the 3D parametric models, conditions or constraints on osculatory orbital or other parameters can be added in the adjustment to take into account the knowledge and the accuracy of the ephemeris or other data, when available. They thus prevent the adjustment from diverging and they also filter the input errors.

Since there are always redundant observations to reduce the input error propagation in the geometric models a least-square adjustment is generally used. When the model equations are non-linear, which is the case for 2<sup>nd</sup>- and higher order non-parametric and parametric models, some means of linearization (series expansions or Taylor's series) must be used. A set of approximate values for the unknown parameters in the equations must be thus initialized:

- To zero for the non-parametric models, because they do not reflect the image acquisition geometry; or
- From the osculatory orbital and sensor parameters of each image for the 3D parametric models.

More information on least-squares methods applied to geomatics data can be obtained in Mikhail (1976) and Wong (1980). The results of this processing step are:

- The parameter values for the geometric model used for each image;
- The residuals in X and Y directions (and Z if more than one image is processed) for each GCP and their root mean square (RMS) residuals;
- The errors and bias in X and Y directions (and Z if more than one image is processed) for each Independent Check Point (ICPs) if any, and their RMS errors; and
- The computed cartographic coordinates for each point, including ETPs and TPs.

When more GCPs than the minimum theoretically required are used, the GCP residuals reflect the modelling accuracy, while the ICP errors reflect the final accuracy. As mentioned previously, this final accuracy is mainly dependent on the geometric model and the number of GCPs used versus their cartographic and image co-ordinates.

When no ICP is available, RMS residuals can be carefully used as an approximation of the final accuracy, only when using 3D parametric models. However, the fact that RMS residuals can be small with 2D/3D non-parametric models does not mean necessarily a good accuracy because these models correct locally at GCPs and the least-square adjustment minimises residuals at GCPs. Errors are still present between GCPs. On the other hand with the use of overabundant GCPs with 3D parametric models, the input data errors (plotting and/or map) do not propagate through the parametric models but are mainly reflected in the GCP residuals due to a global adjustment. Consequently,



it is thus “normal and safe” with 3D parametric models to obtain RMS residuals in the same order of magnitude than the GCP accuracy, but the model by itself will be more precise. In contrast to polynomial methods, which are sensitive to GCP number and spatial distribution (including their elevation), the 3D parametric models are not affected by these factors because it precisely retains the complete viewing geometry, given that there is no extrapolation in planimetry and also in elevation.

### **3.4 Image rectification**

The last step of the geometric processing is the image rectification (Figure 6-4). To rectify the original image into a map image, there are two processing operations:

- A geometric operation to compute the cell coordinates in the original image for each map image cell; and
- A radiometric operation to compute the intensity value or digital number (DN) of the map image cell as a function of the intensity values of original image cells that surround the previously-computed position of the map image cell.

#### **3.4.1 Geometric operation**

The geometric operation requires the two equations of the geometric model with the previously-computed unknowns, and sometimes elevation information. In fact, since 3D parametric models take into account the elevation distortion, a DEM is needed to create more precise ortho-images. The rectification should then be called an ortho-rectification. But if no DEM is available, different altitude levels can be input for different parts of the image (a kind of “rough” DEM) to minimize this elevation distortion. It is then important to have a quantitative evaluation of the DEM impact on the ortho-rectification process, both in term of elevation accuracy for the positioning accuracy and grid spacing for the level of details. This last aspect is more important with high-resolution images because a poor grid spacing when compared to the image spacing could generate artefacts for linear features (wiggly roads or edges). Figures 6-9 and 6-10 give the relationship between the DEM accuracy (including interpolation), the viewing/look angles and the resulting positioning error on VIR and SAR ortho-images, respectively. These curves were mathematically computed with the elevation distortion parameters of a 3D parametric model (Toutin, 1995b). However, they could be also used as approximation for other 3D parametric models and the 3D non-parametric models. One of the advantages of these curves is that they can be used to find any third parameter when the two others are known. It can be useful not only for quantitative evaluation of the ortho-rectification, but to forecast the appropriate input data, DEM or the viewing/look angles, depending of the objectives of the project.

For example (Figure 6-9), with a SPOT image acquired with a viewing angle of  $10^\circ$  and with a 45-m DEM accuracy, the error generated on the ortho-image is 9 m. Inversely, if a 4-m final positioning accuracy for the ortho-image is required with a 10-m DEM accuracy, the VIR image should be acquired with a viewing angle less than  $20^\circ$ . The same error evaluation can be applied to SAR data using the curves of Figure 6-10. As other example, if positioning errors of 60 m and 20 m on standard-1 (S1) and fine-5 (F5)

ortho-images, respectively are required 20-m elevation error, which includes the DEM accuracy and the interpolation into the DEM, is thus sufficient. For high-resolution images (spaceborne or airborne), the surface heights (buildings, forest, hedges) should be either included in the DTM to generate a digital surface model (DSM) or taken into account in the overall elevation error.

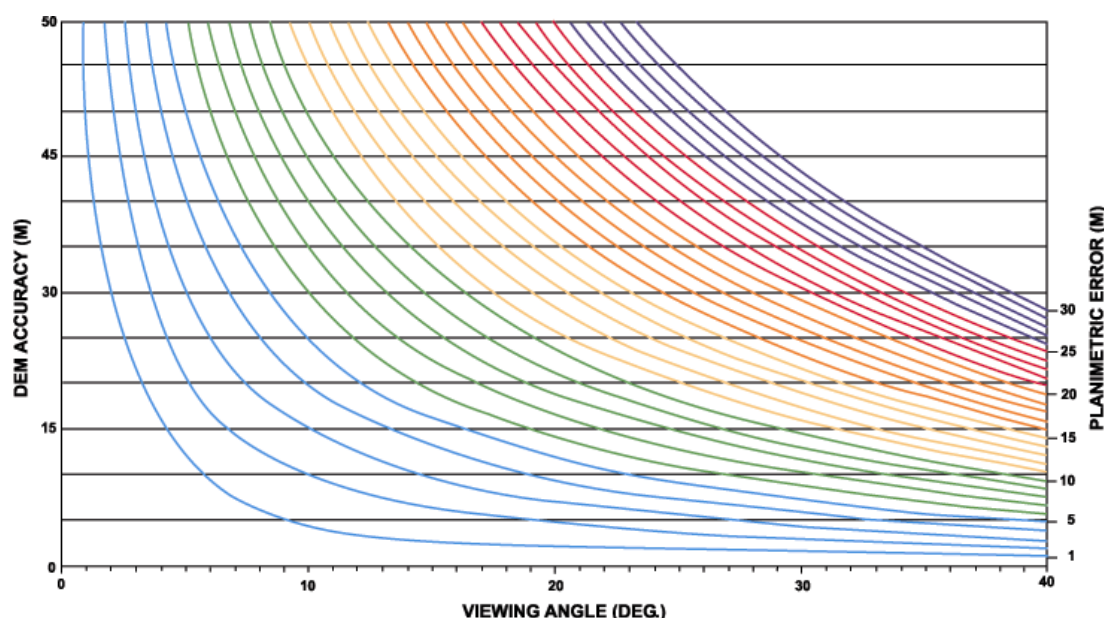


Figure 6-9: Relationship between the DEM accuracy (in metres) the viewing angle (in degrees) of the VIR image, and the resulting positioning error (in metres) generated on the ortho-image (Toutin, 1995b).

Finally, for any map coordinates (X, Y) with the Z-elevation extracted from a DEM when 3D models are used, the original image coordinates (column and line) is computed from the two-resolved equations of the model. However, the computed image coordinates of the map image coordinates will not directly overlay in the original image; in other word, the column and line computed values will be rarely, if never, integer values.

### 3.4.2 Radiometric operation

Since the computed coordinate values in the original image are not integer, one must compute the DN to be assigned to the map image cell. In order to compute the DN to be assigned to the map image cell, the radiometric operation uses a resampling kernel applied to original image cells: either the DN of the closest cell (called nearest neighbour resampling) or a specific interpolation or deconvolution algorithm using the DNs of surrounding cells. In the first case, the radiometry of the original image and the image spectral signatures are not altered, but the visual quality of the image is degraded. In addition to the radiometric degradation, a geometric error of up to half pixel is also introduced. This can caused a disjointed appearance in the map image. If these visual

and geometric degradations are acceptable for the end user, it can be an advantageous solution.

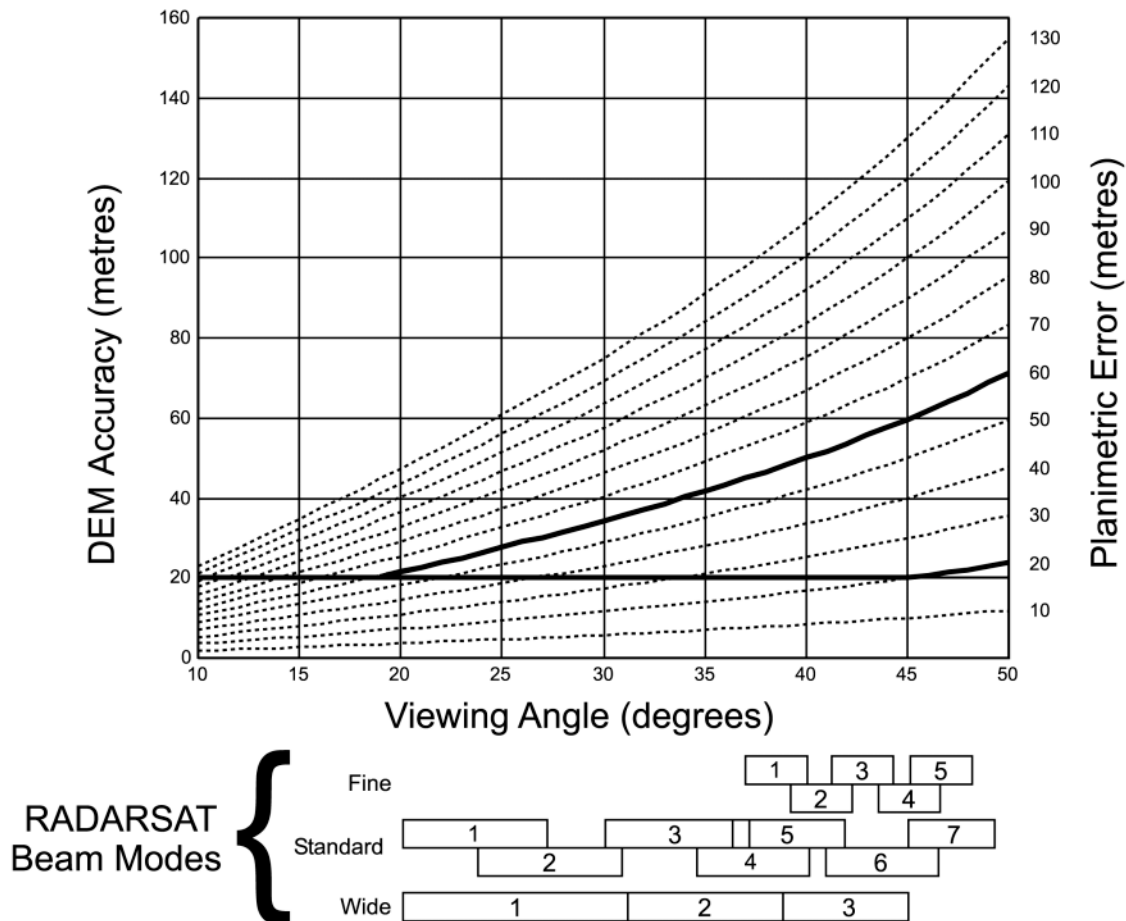


Figure 6-10: Relationship between the DEM accuracy (in metres), the look angle (in degrees) of the SAR image, and the resulting positioning error (in metres) generated on the SAR ortho-image. The different boxes at the bottom represent the range of look angles for each RADARSAT beam mode. (Toutin, 1998).

In the second case, different interpolation or deconvolution algorithms (bilinear interpolation or sinusoidal function) can be applied. The bilinear interpolation takes into account the four cells surrounding the cell. The final DN is then either computed from two successive linear interpolations in line and column using DNs of the two surrounding cells in each direction or in one linear interpolation using DNs of the four surrounding cells. The DNs are weighted as a function of the cell distance from the computed coordinate values. Due to the weighting function this interpolation creates a smoothing in the final map image.

The theoretically ideal deconvolution function is the  $\sin(x)/x$  function. As this  $\sin(x)/x$  function has an infinite domain it cannot be exactly computed. Instead, it can be

represented by piecewise cubic function, such as the well-known cubic convolution. The cubic convolution then computes 3<sup>rd</sup>-order polynomial functions using a 4x4-cell window. DNs are first computed successively in the four-column and -line direction, and the final DN is an arithmetical mean of these DNs. This cubic convolution does not smooth, but enhances and generates some contrast in the map image (Kalman, 1985).

Due to computer improvement these last years, the  $\sin(x)/x$  function can now be directly applied as deconvolution function with different window sizes (generally 8 by 8 or 16 by 16). The computation time with 16 by 16 cell window can be 40 to 80 times more than the computation time for nearest neighbor resampling. The finale image is sharper with more details on features.

All these interpolation or deconvolution functions can be applied to VIR or SAR images. However, they are geometric resampling kernels, not very well adapted to SAR images. Instead, it is better to use statistical functions based on the characteristics of the radar, such as existing adaptive filters using local statistics (Lee, 1980; Lopes *et al.*, 1993; Touzi, 1999). Combining the filtering with the resampling also avoids multiple radiometric processing and transformation, which largely degrades the image content and its interpretation (Toutin, 1995b).

Since interpolation or deconvolution functions transform the DNs and then alter the radiometry of the original image, problems may be encountered in subsequent spectral signature or pattern recognition analysis. Consequently, any process based on the image radiometry should be performed before using interpolation or deconvolution algorithms.

Figures 6-11 and 6-12 are examples of the application of different resampling kernels with Quickbird high-resolution VIR image and RADARSAT-SAR fine mode (F5) image, respectively. Sub-images (200 by 200 pixels) were resampled with a factor of six to better illustrate the variations of the resampling kernels: the Quickbird and RADARSAT resampled image pixels are then 0.10 m and 1.10 m, respectively. Letters A, B, C and D refer to different geometric resampling kernels (nearest neighbour, bilinear, cubic convolution,  $\sin(x)/x$  with 16x16 window), respectively and Letters E and F refer to statistical SAR filters (Enhanced Lee and Gamma), respectively.

For both VIR and SAR images, the nearest neighbour resampling kernel (A) generates “blocky” images with rectangular-edge features, while the bilinear resampling kernel (B) generates fuzzy images with the feeling of “out-of-focus” images. The best results are obtained with the sinusoidal resampling kernels (C & D): even if there are few differences the true sinusoidal function generates sharper features. As example on the Quickbird image (Figure 6-11), the two cars in the front of the houses are better defined in D: the windshield and rear window can be perceived on the car underneath while only the windshield is visible on the other car. It helps to differentiate a car and a station wagon! For the SAR image (Figure 6-12), the two filters (E & F) give even better image appearance than the sinusoidal resampling, due to the fact that the SAR speckle is filtered at the same time.

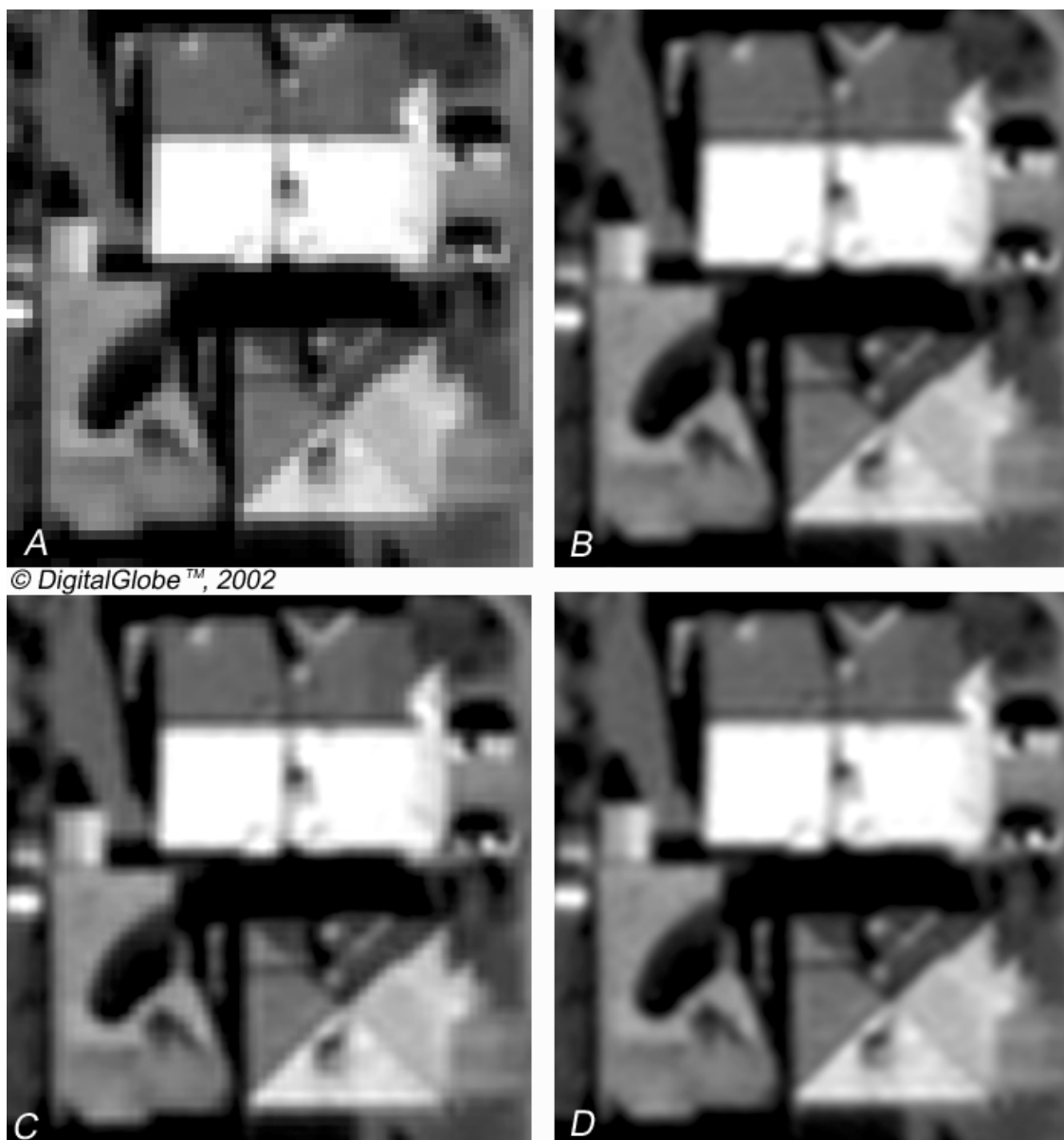
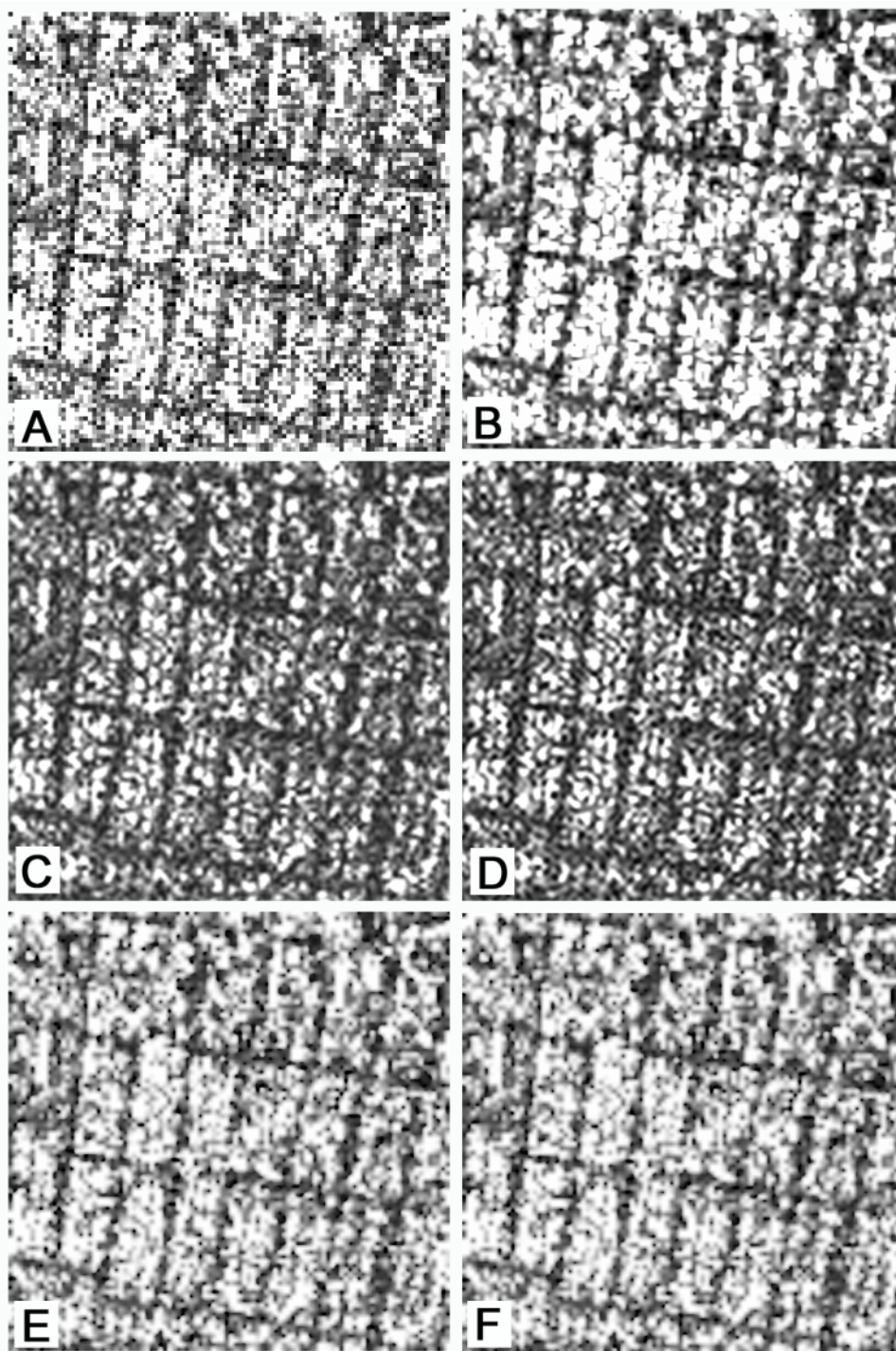


Figure 6-11. Examples of applications of geometric resampling kernels used in the rectification process with a Quickbird image. The sub-images are 350 by 350 pixels with 0.10-m spacing. Letters A, B, C and D refer to different geometric resampling kernels (nearest neighbour, bilinear, cubic convolution,  $\sin(x)/x$  with 16x16 window), respectively and Letters E and F refer to statistical SAR filters (Enhanced Lee and Gamma), respectively. Quickbird Image © Digital Globe, 2001





© Canadian Space Agency, 1997

Figure 6-12. Examples of applications of geometric resampling kernels used in the rectification process with RADARSAT-SAR fine mode (F5) image. The sub-images are 600 by 600 pixels with 1.00-m spacing. Letters A, B, C and D refer to different geometric resampling kernels (nearest neighbour, bilinear, cubic convolution,  $\sin(x)/x$  with 16x16 window), respectively and Letters E and F refer to statistical SAR filters (Enhanced Lee and Gamma), respectively. RADARSAT Images © Canadian Space Agency, 2001

#### 4. CONCLUDING REMARKS

Since the launch of the first civilian remote sensing satellite 30 years ago, the requirements for the geometric processing of remote sensed images have changed drastically. Furthermore, the integration of multi-format data in a digital world requires the highest accuracy possible so as to perform the ortho-rectification of multi-sensor images. While different mathematical functions and solutions can be used, non-parametric solutions are acceptable for low-resolution images while parametric solutions are more appropriate for medium and high-resolution images. Even if 3D non-parametric solutions (mainly with 3D rational functions) have some advantages and can perform well in research environments, 3D parametric solutions have been proven to be more precise and robust and to achieve more consistent results in operational environments than 3D rational solutions. Consequently, they should be the primary choice whenever available. In fact, the mathematical parameterisation of physical models has always been a major issue in scientific research and achievements. When it becomes theoretically and/or practically impossible, however, statistical methods such as 3D rational models can take over.

#### REFERENCES

1. Al-Roussan, N., P. Cheng, G. Petrie, Th. Toutin and M.J. Valadan Zoej, 1997, Automated DEM extraction and ortho-image generation from SPOT level-1B imagery, *Photogrammetric Engineering and Remote Sensing*, Vol. 63, No. 8, pp. 965-974.
2. Bannari, A., D. Morin, G.B. Béné and F.J. Bonn, 1995. A Theoretical Review of Different Mathematical Models of Geometric Corrections Applied to Remote Sensing Images, *Remote Sensing Reviews*, Vol. 13, No. 1, pp. 27-47.
3. Billingsley, F.C., 1983, Data Processing and Reprocessing, in *Manual of Remote Sensing*, 2<sup>nd</sup> Edition, Vol. 1, Editor-in-chief R.N. Colwell, (Falls Church, Virginia, U.S.A., Sheridan Press), pp. 719-722.
4. Caloz, R. et C. Collet, 2001, Précis de télédétection, Volume 3 : Traitements numériques d'images de télédétection, Chapitre 5, Presse de l'Université du Québec, Ste Foy, Québec, Canada, pp. 76-105.
5. Centre National d'Études Spatiales (CNES), 1980, Le mouvement du véhicule spatial en orbite, (Toulouse, France: CNES), 1031 pages.
6. Cheng, Ph. and Th. Toutin, 1998, Unlocking the potential for IRS-1C data, *Earth Observation Magazine*, Vol. 7, No. 3, pp. 24-26.
7. Curlander, J.C., 1982, Location of Spaceborne SAR Imagery, *IEEE Transaction of Geoscience and Remote Sensing*, Vol. GE-22, No. 2, pp: 106-112.

8. Derenyi, E.E., 1970, An Exploratory Investigation into the Relative Orientation of Continuous Strip Imagery, Research Report No. 8, University of New Brunswick, Canada.
9. de Sève, D., Th. Toutin et R. Desjardins, 1996, Evaluation de deux méthodes de corrections géométriques d'images Landsat-TM et ERS-1 RAS dans une étude de linéaments géologiques, *International Journal of Remote Sensing*, Vol. 17, No. 1, pp. 131-142.
10. Dial, G. and Grodecki J., 2002, Block adjustment with rational polynomial camera models, *Proceedings of the ACSM- ASPRS Annual Conference/XXII FIG International Congress*, held in Washington D.C., USA, April 19-26, (ASPRS, USA), CD-ROM.
11. Ebner, H., and Muller F., 1986, Processing of Digital Three Line Imagery Using a Generalized Model for Combined Point Determination, *International Archives of Photogrammetry and Remote Sensing*, Vol. 26 (311), pp. 212-222.
12. Escobal, P.R., 1965, Methods of orbit determination, (Malabar, USA: Krieger Publishing Company), 479 pages.
13. Friedmann, D.E., J.P.Friedel, K.L. Magnusses, K.Kwok and S. Richardson, 1983, Multiple Scene Precision Rectification of Spaceborne Imagery with Few Control Points, *Photogrammetric Engineering and Remote Sensing*, Vol. 49, No. 12, pp. 1657-1667.
14. Gibson, J., 1984, Processing Stereo Imagery from Line Imagers, *Proceedings of 9th Canadian Symposium on Remote Sensing*, (Canada) pp. 471-488.
15. Gracie, G., Bricker, J.W., Brewer, R.K. and R.A. Johnson, 1970, Stereo Radar Analysis, U.S. Engineer Topographic Laboratory, Report No. FTR-1339-1, Ft. Belvoir, VA, U.S.A.
16. Guertin, F., and E. Shaw, 1981, Definition and potential of geocoded satellite imagery products, *Proceedings of the 7th Canadian Symposium on Remote Sensing*, held in Winnipeg, Canada, September 8-11, (Manitoba Remote Sensing Centre, Canada), pp. 384-394.
17. Guran, D.J., 1987, Practical aspects of topographic mapping from SPOT imagery, *Photogrammetric Record*, Vol. 12, No. 69, pp. 349-355.
18. Guichard, H., 1983, Etude théorique de la précision dans l'exploitation cartographique d'un satellite à défilement : application à SPOT, *Société Française de Photogrammétrie et de Télédétection*, Vol. 90, No. 2, pp. 15-26.
19. Guindon, B. and M. Adair, 1992, Analytic Formulation of Spaceborne SAR Image Geocoding and Value-Added Products Generation Procedures Using Digital Elevation Data, *Canadian Journal of Remote Sensing*, Vol. 18, No. 1, pp. 2-12.



20. Hanley, H.B. and C.S. Fraser, 2001, Geopositioning accuracy of IKONOS imagery: Indications from two dimensional transformations, *Photogrammetric Record*, Vol. 17, No. 98, pp. 317-329.
21. Hoffmann, O., and F. Muller, 1988, Combined Point Determination Using Digital Data of three line Scanner Systems. *International Archives of Photogrammetry and Remote Sensing*, Vol. 27 (B11), pp. III / 567 - III / 577.
22. Kalman, L.S., 1985. Comparison of Cubic-convolution Interpolation and Least-squares Restoration for Resampling Landsat-MSS Imagery, *Proceedings of the 51<sup>st</sup> Annual ASP-ASCM Convention: "Theodolite to Satellite"*, Whashington D.C., USA pp. 546-556
23. Khizhnichenko, V.I, 1982, "Co-ordinates transformation when geometrically correcting Earth space scanner images", (in Russian) *Earth Exploration From Space*, No. 5, pp. 96-103.
24. Konecny, G., and W. Schuhr, 1984, Practical Results of Geometric SAR-580, Image Evaluation, *International Archives for Photogrammetry and Remote Sensing*, 25 (A3).
25. Konecny, G., E. Kruck and P. Lohmann, 1986, Ein universeller Ansatz für die geometrische Auswertung von CCD-Zeilenabtasteraufnahmen, *Bildmessung und Luftbildwesen*, Vol. 54, No. 4, pp. 139-146.
26. Konecny, G., Lohmann, P., Engel, H., and E. Kruck, 1987, Evaluation of SPOT Imagery on Analytical Instruments, *Photogrammetric Engineering and Remote Sensing*, Vol. 53, pp. 1223-1230.
27. Kratky, W., 1987, Rigorous Stereophotogrammetric Treatment of SPOT Images. *Comptes- rendus du Colloque International sur SPOT-1 : utilisation des images, bilans, résultats*, Paris, France, pp. 1281-1288.
28. Kratky, W., 1989, On-line aspects of stereophotogrammetric processing of SPOT images, *Photogrammetric Engineering and Remote Sensing*, Vol. 55, No.3, pp. 311-316. W., 1987,
29. La Prade, G.L., 1963, An Analytical and Experimental Study of Stereo for Radar, *Photogrammetric Engineering*, Vol. 29, No. 2, pp. 294-300.
30. Leberl, F.W., 1972, On Model Formation with Remote Sensing Imagery, *Österreichisches Zeitschrift für Vermessungswesen*, Vol. 2, pp. 43-61.
31. Leberl, F.W., 1978, Satellite radargrammetric, *Deutsche Geodactische Kommission*, Munich, Germany, Serie C, 239, 156 pages.

32. Leberl, F.W., 1990. Radargrammetric image processing, Artech House, Norwood, USA, 595 p.
33. Lee, J.S., 1980, Digital Image enhancement and noise filtering by use of local statistics, *IEEE Transactions on Pattern Analysis and Machine Intelligence*, Vol. 2, pp. 165-168.
34. Light, D.L., D. Brown, A. Colvocoresses, F. Doyle, M. Davies, A. Ellasal, J. Junkins, J. Manent, A. McKenney, R. Undrejka and G. Wood, 1980, Satellite Photogrammetry, in *Manual of Photogrammetry* 4<sup>th</sup> Edition, Chapitre XVII, Editor in chief: C.C. Slama, ASP Publishers, Falls Church, USA, pp. 883-977.
35. Lopes, A., Nezry E., Touzi R., Laur H., 1993, Structure Detection and Statistical Adaptive Speckle Filtering in SAR Images, *International Journal of Remote Sensing*, Vol. 14, No 9, pp. 1735-1758
36. Madani, M., 1999, Real-Time Sensor-Independent Positioning by Rational Functions, *Proceedings of ISPRS Workshop on Direct Versus Indirect Methods of Sensor Orientation*, Barcelona, Spain, November 25-26, pp. 64-75.
37. Masson d'Autume, G. de, 1979, Le traitement géométrique des images de télédétection, *Bulletin de la Société Française de Photogrammétrie et de Télédétection*, Vol. 73-74, pp. 5-16.
38. Mikhail, E.M., 1976. Observations and Least Squares, Harper & Row Publishers, New York USA, 497 p.
39. Naraghi, M., Stromberg, W., and Daily, M., 1983, Geometric Rectification of Radar Imagery using Digital Elevation Models, *Photogrammetric Engineering and Remote Sensing*, 49(2), pp. 195-159.
40. Paderes, F.C., Mikhail, E.M., Fagerman, J.A., 1989, Batch and On-line Evaluation of Stereo SPOT Imagery. *Proceedings of the ASPRS - ACSM Convention*, Baltimore, MD, U.S.A., Vol. 3, pp. 31-40.
41. Palà, V. and X. Pons, 1995, Incorporation of Relief in Polynomial-Based Geometric Corrections, *Photogrammetric Engineering & Remote Sensing*, Vol. 61, No. 7, pp. 935-944.
42. Rosenfield, G.H., 1968, Stereo Radar Techniques, *Photogrammetric Engineering*, Vol. 34, No. 6, pp. 586-594.
43. Sakaino, S., Suzuki H., Cheng P., and Toutin Th., 2000, Updating maps of Kazakhstan using stitched SPOT images, *Earth Observation Magazine*, Vol. 9, No 3, pp. 11-13.

44. Salamonowicz, P.H., 1986, Satellite Orientation and Position for Geometric Correction of Scanner Imagery. *Photogrammetric Engineering and Remote Sensing*, Vol. 52, No. 4, pp. 491-499.
45. Savopol, F., A. Leclerc, Th. Toutin et Y. Carbonneau, 1994, La correction géométrique d'images satellitaires pour la Base nationale de données topographiques, *Geomatica*, été, Vol. 48, No. 3, pp. 193-207.
46. Sawada, N., Kikode, M. Shinoda, H., Asada, H., Iwanaga, M., Watanabe, S., and Mori, K., 1981, An Analytic Correction Method for Satellite MSS Geometric Distortion, *Photogrammetric Engineering and Remote Sensing*, Vol. 47, No. 8, pp. 1195-1203.
47. Shu, N., 1987, Restitution géométrique des images spatiales par la méthode de l'équation de colinéarité, *Bulletin de la Société Française de Photogrammétrie et de Télédétection*, Vol. 105, pp. 27-40.
48. Tao, V. and Y. Hu, 2001a, A Comprehensive Study of the Rational Function Model for Photogrammetric Processing, *Photogrammetric Engineering and Remote Sensing*, Vol. 67, No. 12, pp. 1347-1357.
49. Tao, V. and Y. Hu, 2001b, 3-D Reconstruction Algorithms with the Rational Function Model and their Applications for IKONOS Stereo Imagery, *Proceedings of ISPRS Joint Workshop "High Resolution Mapping from Space"*, Hannover, Germany, September 19-21, CD-ROM, pp. 253-263.
50. Toutin, Th., 1983. "Analyse mathématique des possibilités cartographiques du satellite SPOT", *Mémoire du diplôme d'Etudes Approfondies*, Ecole Nationale des Sciences Géodésiques Saint-Mandé, France, pp. 1-74.
51. Toutin, Th., 1985, Analyse mathématique des possibilités cartographiques de système SPOT, *Thèse de Docteur-Ingénieur*, École Nationale des Sciences Géodésiques, (St-Mandé, France: IGN), 163 pages.
52. Toutin, Th., 1995a, Intégration de données multi-sources : comparaison de méthodes géométriques et radiométriques, *International Journal of Remote Sensing*, Vol. 16, No. 5, pp. 2795-2811.
53. Toutin, Th., 1995b. Multi-source Data Integration with an Integrated and Unified Geometric Modelling, *EARSeL Journal "Advances in Remote Sensing"*, Vol. 4, No. 2, pp. 118-129.
54. Toutin, Th., 1996, La correction géométrique rigoureuse : un mal nécessaire pour la santé de vos résultats, *Journal canadien de télédétection*, Vol. 22, No. 2, pp. 184-189.
55. Toutin, Th., 1998. Evaluation de la précision géométrique des images de RADARSAT. *Journal canadien de télédétection*, Vol. 24, No. 1, pp. 80-88.

56. Toutin, Th., 1999, Error tracking of radargrammetric DEM from RADARSAT images, *IEEE-Transactions on Geoscience and Remote Sensing*, Vol. 37, No. 5, pp. 2227-2238.
57. Toutin, Th., 2001, Geometric processing of IKONOS Geo images with DEM, *Proceedings of ISPRS Joint Workshop "High Resolution Mapping form Space"*, Hannover, Germany, September 19-21, CD-ROM, pp. 264-271.
58. Toutin, Th., 2003a, Block adjustment of IKONOS Images, *International Journal of Remote Sensing*, Vol. 24, No. 4, pp. 851-857.
59. Toutin, Th., 2003b, Error tracking in IKONOS geometric processing using a 3D parametric modelling, *Photogrammetric Engineering and Remote Sensing*, Vol. 69, No. 1, pp. 43-51.
60. Toutin, Th., et Y. Carbonneau, 1989. La multi-stéréoscopie pour les corrections d'images SPOT-HRV, *Canadian Journal of Remote Sensing*, Vol. 15, No. 2, pp. 110-119.
61. Toutin, Th. and Y. Carbonneau, 1992, MOS and SEASAT Image Geometric Corrections, *IEEE Transactions on Geoscience and Remote Sensing*, Vol. 30, No. 3, pp. 603-609.
62. Toutin, Th., Y. Carbonneau and L. St. Laurent, 1992, An Integrated Method to Rectify Airborne Radar Imagery using DEM, *Photogrammetric Engineering and Remote Sensing*, Vol. 58, No. 4, pp. 417-422.
63. Toutin, Th. and P. Cheng P 2000, Demystification of IKONOS, *Earth Observation Magazine*, July, Vol. 9, No. 7, pp. 17-21.
64. Toutin, Th., Y. Carbonneau et R. Chénier, 2001, Ajustement de bloc d'images : Exemples avec SPOT, Landsat-7 et IKONOS; *Comptes-rendus du 23<sup>ième</sup> Symposium canadien sur la télédétection*, Ste-Foy, Québec, Canada, 21-24 août, pp. 35-39.
65. Toutin, Th., Y. Carbonneau and R. Chénier, 2001, Block adjustment of Landsat7 ETM<sup>+</sup> images, *Proceedings of ISPRS Joint Workshop "High Resolution Mapping form Space"*, Hannover, Germany, September 19-21, CD-ROM, pp. 281-290.
66. Toutin, Th., R. Chénier et Y. Carbonneau, 2002, 3D Models for High Resolution Images: Examples with QuickBird, IKONOS and EROS, *Proceedings of Joint International Symposium on Geospatial Theory, Processing and Applications (ISPRS, IGU, CIG)*, Ottawa, Ontario, Canada, July 8-12, 2002, CD-ROM.
67. Toutin, Th. and P. Cheng, 2002, QuickBird: A Milestone to High Resolution Mapping, *Earth Observation Magazine*, April, Vol. 11, No. 4, pp. 14-18.

68. Touzi, R., 1999, Speckle filtering of stationary and nonstationary scene signals in SAR imagery, *Proceedings IGARSS'99*, Hamburg, Germany, pp. 1-3.
69. Valadan Zoej, M.J. and G. Petrie, 1998. Mathematical modelling and accuracy testing of SPOT Level-1B stereo-pairs, *Photogrammetric Record*, Vol. 16, No. 91, pp. 67-82.
70. Veillet, I., 1991. Triangulation spatiale de blocs d'images SPOT. *Thèse de Doctorat*, Observatoire de Paris, Paris, France, 101 pages.
71. Westin, T., 1990, Precision Rectification of SPOT Imagery, *Photogrammetric Engineering and Remote Sensing*, Vol, 56, No. 2, pp. 247-253.
72. Wong, K.W., 1980, Basic Mathematics of Photogrammetry, in *Manual of Photogrammetry* 4<sup>th</sup> Edition, Chapter II, Editor in chief: C.C. Slama, ASP Publishers, Falls Church, USA, pp. 37-101.